

Development of Europium Spinel Oxide Dual Biosensors for the Enzymatic detection of Cyclophosphamide and Ifosfamide

Master's Degree Thesis in Biomedical Engineering

Supervisors:

Prof. Alberto Tagliaferro (PoliTo) Prof. Sandro Carrara (EPFL) Dr. Mattia Bartoli (IIT)

Candidate:
Marta Lato

Academic Year 2024-2025

Contents

1	\mathbf{Intr}	oduction	1
	1.1	Electrochemical Sensors	1
	1.2	Biosensors and Electrochemical Detection	4
		1.2.1 Enzyme-Based Biosensors	4
	1.3	Metal Oxide Spinels	5
		1.3.1 Europium	7
	1.4	Cyclophosphamide and ifosfamide detection	8
	1.5	Project Aim	8
2	The	oretical Background	9
	2.1	Fundamentals of Electrochemistry	9
		2.1.1 Nernst Equation	10
		±	12
	2.2	±	12
		v v	12
		V	14
	2.3	1	16
		±	16
		2.3.2 Laviron Equations	16
3	Mat		18
	3.1		18
	3.2	V 1	18
	3.3		19
		1 1	19
		3.3.2 Functionalization with Europium Spinel Oxides and Cy-	
		V	19
	3.4		20
		v v	20
		1 0	21
	3.5	1	21
			21
		, ,	21
		3.5.3 Cyclophosphamide and Ifosfamide Solution	22

	3.6	Electro	ochemical Measurements	23
		3.6.1	Ferro/Ferricyanide Characterization	24
		3.6.2	Cyclophosphamide and Ifosfamide Measurements	25
4	Res	ults ar	nd Discussion	27
	4.1	Mater	ial Characterization	27
		4.1.1	Crystal Structure Analysis (XRD and Raman)	27
		4.1.2	Morphological Analysis (FESEM)	31
	4.2	Electro	ochemical Characterization in Ferro/Ferricyanide	31
		4.2.1	Cyclic Voltammetry (CV) Analysis and Kinetic Parameter	
			Calculation	31
		4.2.2	Cyclophosphamide and Ifosfamide detection without enzymes	38
		4.2.3	Cyclophosphamide Detection with CYP2B6	38
		4.2.4	Ifosfamide Detection with CYP3A4	40
		4.2.5	Comparison of Spinel Europium Oxides	42
	4.3	Valida	tion in Human Serum	43

List of Figures

1.1	Schematic diagram of a sensor. The components are receptor, transducer, electronic system, and display.	1
1.2	Comparison of two electrochemical sensors with working, reference and auxiliary electrode materials indicated.	3
1.3	Biomolecules, organic or inorganic materials: examples of materials for the functionalization of screen-printed electrodes	4
1.4	Schematic representation of the spinel structure with the general formula AB_2O_4 , where A and B are metal cations reproduced	-
	from reference[17]	6
1.5	Schematic representation that summarize the project	8
2.1	Illustration of homogeneous (a) and heterogeneous (b) electron transfer processes [29] . The energy difference between molecular	
0.0	orbitals or electrodes controls electron transfer	10
2.2	Cyclic voltammetry illustration showing both the voltammogram	13
2.3	(a) and the potential waveform (b). Reprinted from [29] Overview of the measurement properties of the Differential Pulse	13
2.0	Voltammetry (DPV) command, showing the potential waveform with key parameters such as start potential, stop potential, step potential, modulation amplitude, modulation time, interval time, and measurement times for base and pulse currents. Reprinted	
	from [33]	14
2.4	Randles equivalent circuit: solution resistance (R_s) in series with the parallel combination of charge transfer resistance (R_{ct}) and	
	double-layer capacitance (C_{dl})	16
3.1	Schematic representation of the autocombustion synthesis method for europium spinel oxides	19
3.2	Schematic illustration of the dual sensor setup. The right working	
	electrode is modified with europium oxide nanoparticles only, while the left working electrode is modified with europium oxide	
9 9	nanoparticles functionalized with cytochrome P450 enzyme Electrochemical measurement setups: (a) general AUT302N.MBA	20
3.3	potentiostat configuration, and (b) dipping configuration with SPCE, CE, and RE.	24
	or on, and in	24

4.1	XRD pattern of the CuEu ₂ O ₄ sample showing characteristic spinel	
	reflections and minor Eu_3O_4 impurity	28
4.2	XRD pattern of the ZnEu ₂ O ₄ sample with major spinel peaks	
	and secondary phases ZnO and Eu_2O_3	28
4.3	XRD pattern of the CoEu ₂ O ₄ sample indicating spinel phase with	
	CoO and Eu_2O_3 impurities	28
4.4	Raman spectrum of the CuEu ₂ O ₄ sample showing characteristic	
	vibrational modes and impurity contributions	29
4.5	Raman spectrum of the CoEu ₂ O ₄ sample indicating major vibra-	
	tional modes and minor Eu_2O_3 impurity	30
4.6	Raman spectrum of the ZnEu ₂ O ₄ sample with spinel vibrational	
	modes and ZnO secondary phase	30
4.7	FESEM images of europium-based spinel oxide nanoparticles	31
4.8	Elettrochemical characterization in ferro/ferricianyde: bare elec-	
	trode e $\operatorname{ZnEu_2O_4}$	35
4.8	Elettrochemical characterization in ferro/ferricianyde CuEu ₂ O ₄ e	
	$CoEu_2O_4$	36
4.9	EIS Bode plots of the electrodes in a ferro/ferricyanide solution;	
	three-electrode configuration for all materials except the bare	
	electrode	37
4.10	Calibration curves for the three europium spinel oxide materials:	
	(a) ZnEu ₂ O ₄ , (b) CoEu ₂ O ₄ , and (c) CuEu ₂ O ₄ with CYP2B6	
	enzymes for cyclophosphamide detection	39
4.11	Calibration curves for the three europium spinel oxide materials:	
	(a) ZnEu ₂ O ₄ , (b) CoEu ₂ O ₄ , and (c) CuEu ₂ O ₄ with CYP3A4 for	
	ifosfamide detection	41
4.12	Peak current vs. concentration for CoEu ₂ O ₄ modified electrodes	
	with the corresponding cytochrome P450 enzymes. (a) Cyclophos-	
	phamide with CYP2B6, (b) Ifosfamide with CYP3A4	42
4.13	Calibration curves for cyclophosphamide (left) and ifosfamide	
	(right) obtained from DPV measurements in human serum, show-	
	ing linear response in the tested concentration ranges	44

List of Tables

1.1	Main ferrite synthesis methods with corresponding advantages and disadvantages. Adapted from [21]	7
3.1 3.2	Yield of europium spinel oxides	19
3.3	required to prepare target concentrations ranging from 5 to 100 μ M Volumes of 1 mM ifosfamide stock solution and PBS required to	22
3.4	prepare target concentrations ranging from 10 to 120 μM Experimental parameters for EIS measurements	23 25
3.5	DPV parameters used for cyclophosphamide and ifosfamide mea-	
3.6	Surements	25
3.7	surements	26
	in droplet configuration measurements	26
4.1 4.2	Linear regression of peak currents vs. $\sqrt{\nu}$	33
	Linear regression of peak potentials vs. $\ln \nu$ and potential difference ΔE_p	33
4.3	Summary of kinetic parameters and relative electroactive surface area	33
4.4 4.5	Summary of electrochemical characteristics of the materials Summary of the electroanalytical performance of ZnEu ₂ O ₄ , CuEu ₂ O ₄ .	34
1.0	and CoEu ₂ O ₄ modified electrodes. Reported values include the slope of the calibration curve, the relative sensitivity, the coeffi-	,
4.0	cient of determination (R^2) , and the limit of detection (LOD)	40
4.6	Summary of the electroanalytical performance of $ZnEu_2O_4$, $CuEu_2O_4$ and $CoEu_2O_4$ modified electrodes. Reported values include the	,
	slope of the calibration curve, the relative sensitivity, the coefficient of determination (R^2) , and the limit of detection (LOD).	40
4.7	Qualitative comparative summary of europium-based spinel oxides with CYP3A4 (ifosfamide) and CYP2B6 (cyclophosphamide)	43
4.8	Concentration ranges of cyclophosphamide and ifosfamide solu-	40
	tions tested in human serum	43

4.9 Sensitivity and determination coefficients of DPV calibration curves for cyclophosphamide and ifosfamide in serum are shown in the table. The measurements were performed using three CuEu2O4 electrodes functionalized with CYP2B6 for cyclophosphamide detection and CYP3A4 for ifosfamide detection. 4-

Abstract

Electrochemical sensors convert chemical information into electrical signals, allowing biomolecules to be detected even in complex samples. Nanostructured metal oxides with spinel structures are especially useful due to their high catalytic activity, large surface area, and enhanced electron transfer, which improve sensor sensitivity and selectivity. In this study, europium-based spinel oxide nanoparticles doped with copper, cobalt, and zinc (CoEu₂O₄, CuEu₂O₄, ZnEu₂O₄) were prepared using an autocombustion method in order to exploit the electronic properties of europium which thanks to its f-orbital configuration should facilitate electron exchange. The morphological and crystal structures of the nanoparticles were investigated: Field Emission Scanning Electron Microscope (FESEM) analysis confirmed that the particles were uniform and well dispersed, while X-ray diffraction (XRD) demonstrated the formation of a highly crystalline cubic spinel structure and Raman spectroscopy provided additional confirmation of the chemical composition and structural quality of the material. The electrochemical properties of the different materials were studied using cyclic voltammetry (CV) in ferro/ferricyanide solutions with commercial single sensor screen-printed carbon electrodes (SPCE Metrohm DRP-11L) at various scan rates (25 – 100mV/s). The quasi-reversible electron transfer observed allowed the calculation of electron transfer coefficients and diffusion constants by applying Laviron's model and the Randles-Sevčík equation. Electrochemical impedance spectroscopy (EIS) provided insight into surface properties and charge transfer resistance. Nanoparticles were deposited via drop-casting on the commercial dual screen-printed carbon electrodes (DRP-X1110). Two types of sensors were developed: one with only nanomaterials and another combining nanomaterials with selective enzymes CYP2B6 and CYP3A4, which metabolize cyclophosphamide and ifosfamide, respectively. The sensors without enzymes showed almost no response, in contrast, sensors incorporating enzymes showed significant and stable responses due to the enzymatic reaction required for detecting the prodrugs. The developed biosensors were tested in phosphate-buffered saline (PBS) at drug concentrations of 5–100 µM (cyclophosphamide) and 10–120 µM (ifosfamide), revealing copper europium oxide (CuEu₂O₄) as the most reliable sensor, showing good sensitivity and a linear detection range. The sensitivity values were $1.37 \pm 0.05 \, \text{nA}/\mu\text{M} \cdot \text{mm}^2$ for CuEu_2O_4 combined with CYP2B6 for cyclophosphamide detection, and $1.66 \pm 0.05 \,\mathrm{nA}/\mu\mathrm{M}\cdot\mathrm{mm}^2$ for $\mathrm{CuEu_2O_4}$ combined with CYP3A4 for ifosfamide detection. Although cobalt europium oxide exhibited higher sensitivity in both system it saturated at higher concentration values. For this reason, CuEu₂O₄ was chosen for further evaluation in human serum to simulate biological conditions.

In conclusion, europium spinel oxides, especially $CuEu_2O_4$, show promising results for developing dual electrochemical biosensors for key drug targets. Future studies will aim to expand detection capabilities to other drugs, supporting the advancement of point of care technology for personalized medicine.

Chapter 1

Introduction

1.1 Electrochemical Sensors

A sensor is a device designed to convert physical or chemical quantities into a signal that can be detected and analyzed [1] .

It is consisted in two main components the receptor and the transducer. The first element is the part of the sensor that interacts with the target molecule, leading a change in its properties. The second element then converts this change into a measurable electrical signal.

Depending on the physical quantity measured, the transducer can be electrochemical, optical, piezoelectric, or thermal. Then the signal is processes to analyze and display the output signal (Figure 1.1).

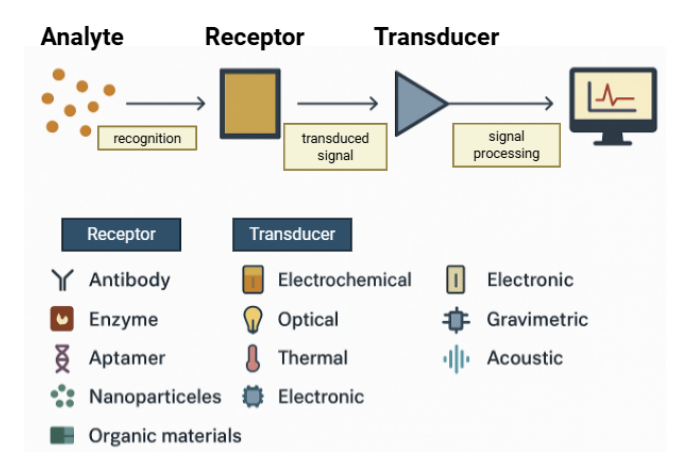


Figure 1.1: Schematic diagram of a sensor. The components are receptor, transducer, electronic system, and display.

Among the different transducer types, electrochemical sensors are the most

frequently [2] .An electrochemical sensor uses a transducer that transforms chemical information into an electrical signal generated by the interaction between the analyte and the sensor. They are commonly divided into three categories according to their output signal:

- Potentiometric sensors, which measure changes in electrode potential without current flow;
- Amperometric sensors, which record current changes at a fixed applied potential;
- Conductometric sensors, which detect changes in the conductivity of the material between electrodes [3].

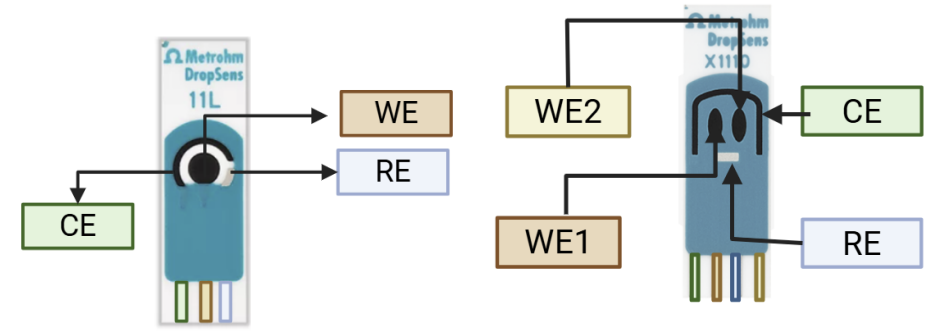
Amperometric sensors typically apply a constant voltage, instead if the voltage varies over time these sensors are called voltammetric. When a potential is applied, redox reactions occur at the electrode electrolyte interface, causing an electron transfer which is a current that is proportional to the analyte concentration.[3] They are used to several advantages compared to traditional analytical methods which generally require expensive equipment, trained people and longer processing times. In contrast, electrochemical sensors offer high sensitivity and selectivity and fast response times [4], affordable instrumentation and easy miniaturization. Also they can be modified to enhance performance. Electrochemical sensors have many applications including clinical diagnostics, food safety and industrial control. One of most used electrochemical sensor are Screen-Printed Electrodes (SPEs) fabricate by screen printing. SPEs consist of multiple electrodes fabricated on a glassy or ceramic substrate using conductive inks made from carbon or noble metals. A typical SPE design includes three electrodes: the working electrode (WE), the counter or auxiliary electrode (CE), and the reference electrode (RE), arranged in a three-electrode cell configuration [4]. There are also SPCE with two working electrode. Both are shown in Figure 1.2.

Applying a potential difference between the working and reference electrodes the redox reactions begin . These reactions cause electron flow between the working and counter electrodes, which is recorded over time.

SPCEs have small sizes, enabling smaller sample volumes while achieving detection limits down to picomolar levels . SPEs are versatile, detecting both organic molecules such as DNA , as well as inorganic ions like copper and mercury

.

The selection of materials and ink composition, along with the working electrode's surface properties, are critical to sensor performance and depend on the intended analysis [5], [6]. Bare SPEs made from carbon or gold are common due to favorable electron transfer kinetics, low cost, and biocompatibility. However, they typically lack sufficient selectivity and sensitivity for detecting analytes present at low concentrations [7] One advantage of screen-printing technology is the possibility to easy modify them to improve their performances. Sensitivity, defined as the slope of the calibration curve for a target analyte, is



(a) SPCE 11L: 1 WE, Carbon WE, Silver RE, Carbon AE

(b) X1110 Dual: 2 WEs, Carbon WEs (d1=0.40 cm, d2=0.17 cm), Silver RE, Carbon AE

Figure 1.2: Comparison of two electrochemical sensors with working, reference and auxiliary electrode materials indicated.

a crucial characteristic. A highly sensitive sensor can detect minor changes in analyte concentration with a clear response. This property is linked to the limit of detection (LoD), which is the lowest analyte concentration that can be reliably distinguished from background noise [3]. Specificity refers to the sensor's ability to identify the target analyte in the presence of other interfering species [3].

For practical applications, an optimal sensor should combine high sensitivity with a sufficiently low LoD.

A sensor with good specificity therefore minimizes false responses and ensures accurate detection in complex environments.

To enhance sensor properties, the working electrode's surface area can be increased. Recently, many studies have combined electrochemical sensors with biotechnology and nanotechnology to optimize the performances for specific uses . Organic or inorganic substances may be incorporated into the conductive ink during fabrication or added later on the electrode's surface. Functionalizing electrodes with biological molecules, polymers or nanomaterials improves electrocatalytic activity, conductivity and electron transfer efficiency which results in better sensor performance [8].

Adding biomolecules such as enzymes or antibodies to the SPE surface improves the sensor's specificity, as these molecules catalyze particular reactions and they can reduce interferences. Similarly, nanomaterials like carbon nanotubes or metal nanoparticles increase sensitivity by enlarging the electrode's active surface and enhancing conductivity [[3]]. Figure 1.3 shows examples of biomolecules, organic and inorganic materials used for SPE functionalization.

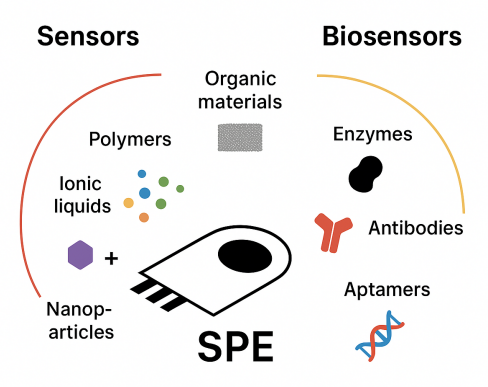


Figure 1.3: Biomolecules, organic or inorganic materials: examples of materials for the functionalization of screen-printed electrodes

1.2 Biosensors and Electrochemical Detection

Biosensors are a group of chemical sensors where a biological molecule (enzyme, antibody, receptor) acts as the recognition element. These biological components interact with the analyte, and the transducer converts the biochemical event into an electrical signal [9]. Biosensors are known for their high selectivity and sensitivity and real time on site analytical capability that make them useful in medical diagnostics, genetics, environmental monitoring, and food safety [10].

In the field of electrochemical sensing, one of the main problems of non-biologic nanomaterials is the lack of specificity towards the target molecules instead the biomolecules guarantee high selectivity and specificity during the analysis process.

Catalytic biosensors use biomolecules such as enzymes or proteins that catalyze specific chemical reactions. In this case, the bioreceptor reacts chemically with the analyte producing a reaction product. The transducer detects the concentration of this product and, using a known correlation, calculates the original analyte concentration in the sample.

On the other hand, affinity biosensors are based on bioreceptors like antibodies, binding proteins, or aptamers, which bind selectively and specifically to the target analyte. In this case the transducer measures the amount of the analyte directly based on this binding interaction .

1.2.1 Enzyme-Based Biosensors

Enzyme modified biosensors are a significant class within biosensor technology due to their higher specificity and catalytic properties. These sensors utilize enzymes as bioreceptors which catalyze specific chemical reactions with high selectivity towards their substrates [11]. The enzyme substrate interaction leads

to the conversion of the target analyte into a detectable product, which the transducer measures to provide an electrical signal proportional to the analyte concentration.

A important advantage of enzymatic biosensors is the natural selectivity of enzymes which allows the sensor to distinguish the target molecule in complex sample matrices with interfering substances. Enzymes are also efficient biological catalysts capable of accelerating reaction rates without being consumed that make continuous monitoring possible [12],[13].

However, enzymatic biosensors have some limitations such as they are sensitive biomolecules which need specific environmental conditions like optimal pH, temperature, and humidity to maintain their activity and stability. In addition, free enzymes lost activity over time and denature [14].

To address improving enzyme stability and sensor robustness they can be immobilized on nanostructured materials or nanoparticles provide a supportive matrix that enhances enzyme stability, preserves biological activity and facilitates efficient electron transfer between the enzyme and the electrode.

The integration of nanomaterials not only stabilizes the enzyme but can also increase the effective surface area of the electrode, improving sensitivity and lowering limits of detection. Enzymes are commonly used as recognition elements in electrochemical biosensors because of their high selectivity and sensitivity. Among them, cytochromes P450 (CYPs) are especially interesting because of their properties, which make them very suitable for enzyme-based detection in amperometric biosensors, particularly for drug monitoring.

The cytochrome P450 enzyme contains a heme group with an iron atom. When the enzyme interacts with the drug (substrate), the drug binds near the heme group, causing a change in the enzyme structure.

The iron in the heme group is reduced and binds oxygen, which allows the enzyme to catalyze the chemical transformation of the drug [15], [16].

This reaction changes the oxidation state of the iron, enabling direct electron transfer to the electrode surface. The resulting current is proportional to the drug concentration, allowing its detection and quantification. Enzymatic biosensors also benefit from advances in transducer technology, where integrating miniaturized and lowmcost electronic components enables the development of portable, user friendly devices suitable for point of care testing . The aim in biosensor design is to combine enzyme selectivity with reproducible and rapid signal transduction systems that enable precise and reliable analyte quantification across various fields including medical diagnostics, environmental monitoring and food safety.

1.3 Metal Oxide Spinels

Metal oxide nanoparticles structure are a class of materials highly studied for their versatile electrochemical properties. The general formula for these spinel oxides is AB₂O₄, where A and B represent metal cations. The cations can placed in two types of sites: the tetrahedral (A) sites and the octahedral (B) sites. The spinel structure is based on a face-centered cubic (FCC) lattice made of 32 oxygen anions. In this structure, there are 64 tetrahedral sites, which are spaces surrounded by four oxygen anions, and 32 octahedral sites, spaces surrounded by six oxygen anions. Shown in Figure 1.4

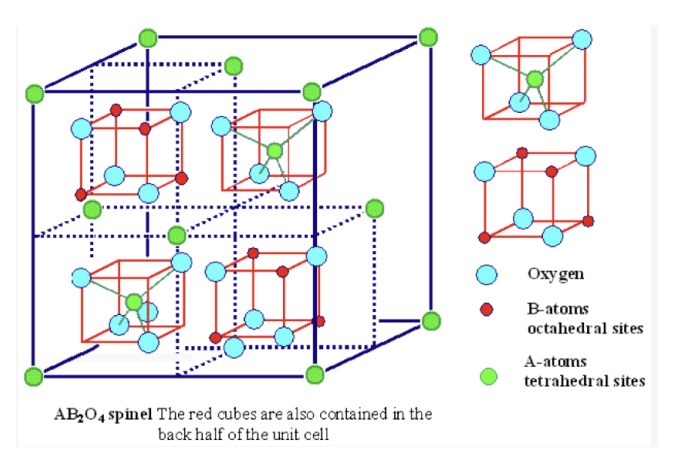


Figure 1.4: Schematic representation of the spinel structure with the general formula AB_2O_4 , where A and B are metal cations reproduced from reference[17]

Depending on which cations occupy the tetrahedral and octahedral sites, the spinel can be normal, inverse, or partially inverse.

In the normal spinel structure, divalent metal ions occupy the tetrahedral sites while trivalent metal ions occupy the octahedral sites. Zinc ferrite $(ZnFe_2O_4)$ is a classical example of this arrangement. Instead in the inverse spinel structure, half of the trivalent ions occupy the tetrahedral sites, and the divalent metal ions with the remaining trivalent ions populate the octahedral sites. Nickel ferrite $(NiFe_2O_4)$ is a typical inverse spinel. It is also possible the mixed spinel structure where cation distribution between tetrahedral and octahedral sites is partial and influenced by factors such as ionic size, valence state, lattice energy and electrostatic interactions.

Metal oxide nanoparticles exhibit enhanced properties compared to their bulk materials. Surface to volume ratio, tunable magnetic and electrical behaviors, and amplified catalytic activity increased. In particular, spinel ferrite nanoparticles demonstrate advantageous electrocatalytic properties for applications like electrochemical sensing. Their high surface area amplifies active sites for analyte adsorption, while the electron transfer dynamics at the electrode interface are improved by their conductive metal oxide structure. Such properties enable sensors with higher sensitivity, selectivity, faster response times and lower detection limits [18].

Many synthesis methods are used to produce ferrite nanoparticles which can be categorized into top down and bottom up approaches.

Top down methods involve breaking down bulk materials into nanoscale parti-

cles, while bottom up techniques build nanoparticles from molecular or atomic precursors.

One used bottom up technique is the autocombustion method [19], appreciated for its simplicity, cost-effectiveness, and rapid processing . This method is based on a fast exothermic reaction between metal precursors, such as nitrates, and an organic fuel like urea. The characteristics of the resulting ferrite nanoparticles depend on factors such as the fuel type and the fuel to precursor ratio. Autocombustion is extensively applied in producing ceramic materials, composites, and ferrimagnetic nanomaterials, offering advantages like efficient synthesis, short preparation time, low cost. However, it requires high combustion temperatures .

Table 1.1 summarizes other common synthesis methods[20] for ferrite nanoparticles, highlighting their main advantages and drawbacks.

Table 1.1: Main ferrite synthesis methods with corresponding advantages and disadvantages. Adapted from [21]

Method	Advantages	Disadvantages
Hydrothermal	High crystallinity	Requires strict conditions
Co-precipitation	Low cost, high purity	Possible impurities, long reaction times
Sol-gel	Ultra-fine, uniform particles	Expensive, toxic reagents
Template	Controlled growth	Complex template handling
Electrospinning	Porous particles, large surface	Use of toxic chemicals, multiple param-
	area	eters to control

The choice of synthesis method modify the size, morphology, and surface characteristics of ferrite nanoparticles, which influence their properties and performance in sensing applications [19],[18]. Also the nanoparticle morphology impacts how the electroactive layer interfaces with analytes, influencing the overall sensor response.

1.3.1 Europium

Europium (Eu) is a rare earth element with partially filled 4f orbitals, which are well shielded by the outer 5s and 5p electrons. This makes europium ions very stable and allows them to keep their electronic states even in complex oxides [22]. In the AEu_2O_4 spinel oxide, europium helps control the local electron density around the cation sites. This is important for studying charge transfer and improving the material's electrochemical properties. For these reasons, europium was chosen as the dopant in AEu_2O_4 spinel oxides.

1.4 Cyclophosphamide and ifosfamide detection

Cyclophosphamide and ifosfamide are two used chemotherapy drugs belonging to the alkylating agents class. Both require metabolic activation by cytochrome P450 enzymes, primarily the isoforms CYP2B6 and CYP3A4. These enzymes catalyze the conversion of the prodrugs into their active metabolites responsible for their anticancer effects. Specifically, cyclophosphamide is bioactivated mainly by CYP2B6 [23], which converts it into 4-hydroxycyclophosphamide, leading to the formation of the cytotoxic metabolite phosphoramide mustard [24],[25]. Ifosfamide undergoes a similar pathway, predominantly mediated by CYP3A4[26], which converts it into 4-hydroxyifosfamide, and subsequently into isophosphoramide mustard [27],[28]. These activated metabolites are responsible for DNA alkylation and cancer cell death.

1.5 Project Aim

The aim of this thesis is to develop and study electrochemical sensors based on dual screen-printed carbon electrodes modified with europium oxide for the detection of drugs. A dual sensor configuration was used to improve sensing performance, where one working electrode was left without enzyme modification while the other was functionalized with enzyme and europium oxide material. Two different enzymes were used: CYP2B6 for the detection of cyclophosphamide, and CYP3A4 for the detection of ifosfamide.

Since not all europium spinel oxides have been studied in the literature, the first part of this work focused on the synthesis and detailed characterization of these materials. The best performing europium oxide sensor was then tested and validated in serum samples.

The final goal is to contribute to the development of point-of-care devices for personalized medicine by creating reliable and sensitive sensors capable of detecting important drugs. This study will help to understand the benefits of europium oxide in electrochemical sensing and support future applications in healthcare diagnostics.

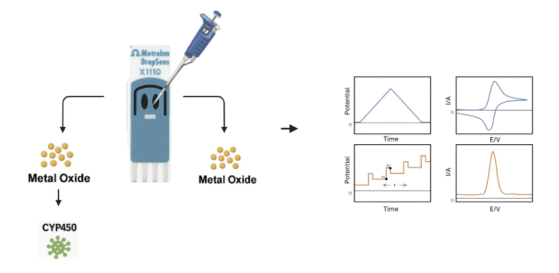


Figure 1.5: Schematic representation that summarize the project

Chapter 2

Theoretical Background

2.1 Fundamentals of Electrochemistry

Electrochemistry is the study of chemical reactions that involve the movement of electrons and how these reactions produce electrical current. Important concept is the redox reaction, where one molecule called the donor gives electrons to another molecule called the acceptor. This causes the donor to lose electrons, oxidation, and the acceptor to gain electrons ,reduction. The overall reaction can be written as:

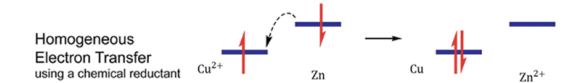
$$Donor + Acceptor \rightarrow Donor^+ + Acceptor^-$$

Redox reactions happen in two main ways. The first is called homogeneous electron transfer, where the electron moves between two molecules in the solution. This happens because the donor's electrons in its highest occupied molecular orbital (HOMO) have more energy than the acceptor's lowest unoccupied molecular orbital (LUMO), so electrons move from HOMO to LUMO 2.1a.

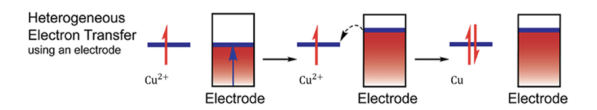
The second type is heterogeneous electron transfer, where electrons move between a molecule in solution and an electrode surface. In this case, the electrode's electron energy can be changed by applying a voltage using a device called a potentiostat [[21]. This allows control of the electron flow from the electrode to the molecule's LUMO or vice versa 2.1b.

In both cases, the difference in energy between the orbitals or between the electrode and the molecule controls whether the electron transfer happens. This study focuses on the heterogeneous electron transfer, which looks at redox reactions happening between an electrode and molecules in the solution.

For example, in an electrochemical cell with a working electrode (WE) and a reference electrode (RE), when the right voltage is applied, the redox reaction of a molecule on the WE produces a flow of electrons. This flow is measured as an electric current between the WE and the counter electrode (CE), completing the circuit[29]. When redox reactions involve organic molecules like enzymes, the process is often different because there is no direct transfer of charge just between



(a) Homogeneous electron transfer where electron moves between two molecules. A is the acceptor and D is the donor. Electrons flow from HOMO of donor to LUMO of acceptor.



(b) Heterogeneous electron transfer where electron moves between an electrode and a molecule. Electrode electron energy is controlled by a potentiostat.

Figure 2.1: Illustration of homogeneous (a) and heterogeneous (b) electron transfer processes [29] . The energy difference between molecular orbitals or electrodes controls electron transfer.

atoms. Instead, the reactions are described as interactions between electron rich (nucleophiles) and electron poor (electrophiles) parts of molecules. Sometimes, redox reactions involve both organic molecules and inorganic materials. For example, in the case of cyclophosphamide reduction with the help of CYP P450 enzymes and spinel oxide nanoparticles, the electron transfer begins at the surface of the carbon electrode. The nanoparticles support and accelerate this transfer, creating a more efficient path for the reaction. The enzyme then reduces the drug in the presence of oxygen, making the reaction selective for the substrate.

2.1.1 Nernst Equation

The Nernst equation describes the relationship between the electrical potential of an electrochemical cell and the concentrations of the oxidized and reduced forms of a chemical species at equilibrium. It quantifies how the cell potential E depends on temperature, reaction conditions, and the ratio of species concentrations, written in the Equation (2.1).

$$E = E^0 + \frac{RT}{nF} \ln \frac{a_{\text{Ox}}}{a_{\text{Red}}}$$
 (2.1)

where E^0 is the standard electrode potential, R the gas constant, T the absolute temperature, n the number of electrons transferred, F the Faraday constant, and a_{Ox} and a_{Red} represent the activities of the oxidized and reduced species, respectively.

In practical applications, activity coefficients are often approximated by concentrations (c_{Ox} , c_{Red}) for simplicity, giving Equation (2.2) [30].

$$E = E'^0 + \frac{RT}{nF} \ln \frac{c_{\text{Ox}}}{c_{\text{Bed}}}$$
 (2.2)

Here, $E^{\prime0}$ is the formal potential, which reflects the specific experimental conditions and is commonly used instead of the standard potential. This equation allows prediction of the electrochemical system behavior when changing species concentrations or applied potential, helping to understand and control redox processes.

Electrode Reactions and Redox Kinetics

An electrode reaction involves electron transfer between the electrode surface and the analyte species in solution. For a species O undergoing reduction, electrons flow from the electrode to convert O into its reduced form R:

$$O + ne^- \to R$$
 (2.3)

This process includes several stages: transport of O to the electrode surface, electron transfer, chemical transformation, and removal of R from the interface.

The rate of electron transfer is affected by factors such as the applied electrode potential, the chemical nature of the species and the physical properties of the electrode surface. Redox kinetics are characterized by two main factors: the speed of electron transfer and the transport rates of reactants and products to and from the electrode surface.

For a single electron redox process:

$$O + e^{-}[k_{\rm ox}]k_{\rm red}R \tag{2.4}$$

the anodic (oxidation) and cathodic (reduction) current densities can be described by Equations (2.5) and (2.6):

$$i_a = -FAk_{\rm red}c_{\rm Ox,surf} \tag{2.5}$$

$$i_c = FAk_{\rm ox}c_{\rm Red,surf}$$
 (2.6)

Here, A is the electrode area, $c_{\text{Ox,surf}}$ and $c_{\text{Red,surf}}$ are surface concentrations, and k_{red} , k_{ox} are the rate constants for reduction and oxidation, respectively. Positive cathodic current corresponds to reduction instead negative anodic current to oxidation.

When electron transfer is fast, the system is reversible and surface concentrations follow the Nernst equation. If transfer is slow, the reaction becomes quasi reversible or irreversible, requiring larger driving potentials and affecting voltammetric measurements.

2.1.2 Mass Transport and Fick's Laws

The kinetics of a redox reaction at an electrode are influenced by how the reactants and products move in the solution. Mass transport controls the supply of reactant species (O) to the electrode and the removal of product species (R) from it. The main mechanisms for mass transport are:

- **Diffusion**: movement caused by concentration gradients.
- Migration: movement due to electric field gradients.
- Convection: bulk solution movement driven by temperature or pressure differences.

In many electrochemical experiments, including the ones discussed during this thesis, convection is avoided by working in unstirred solutions and migration is minimized by adding a large concentration of inert supporting electrolyte. Therefore, diffusion is the dominant transport mechanism in these cases.

Diffusion is described by Fick's laws:

• Fick's First Law states that the diffusion flux \vec{J} is proportional to the concentration gradient (Equation (2.7)):

$$\vec{J} = -D\nabla c(x,t) \tag{2.7}$$

where D is the diffusion coefficient and c(x,t) the concentration at position x and time t. The negative sign indicates diffusion occurs from high to low concentration.

• Fick's Second Law governs the change in concentration over time due to diffusion (Equation (2.8)) [23]:

$$\frac{\partial c(x,t)}{\partial t} = D \frac{\partial^2 c(x,t)}{\partial x^2}$$
 (2.8)

This equation predicts how concentrations evolve spatially and temporally near the electrode surface during redox reactions.

The electrochemical current measured is related to the flux of reacting species at the electrode surface and it depends on the electrode area, the diffusion coefficient, and the rate of concentration change near the electrode. Understanding these transport phenomena is fundamental to interpreting electrochemical data and designing sensors and devices.

2.2 Electrochemical Techniques

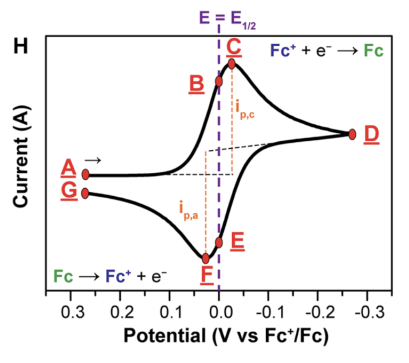
2.2.1 Cyclic Voltammetry

Cyclic voltammetry (CV) is one of the most employed electrochemical methods for the investigation of redox-active systems. In CV, a triangular potential

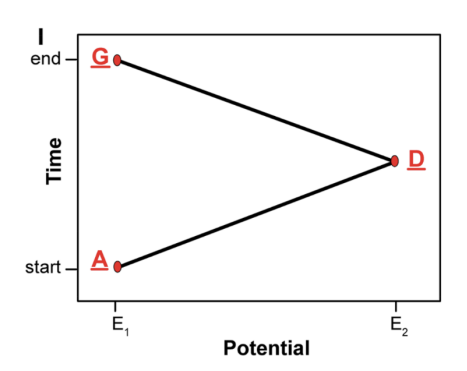
waveform (2.2b) is applied between the working and reference electrodes by means of a potentiostat, while the current is simultaneously recorded at the working electrode. During the scan, the potential is switch from an initial value E_1 to potential E_2 , then, the scan is reversed back to E_1 Figure 2.2b. This cyclic variation of the applied potential induces the oxidation and reduction of the electroactive species present in solution in a repetitive way.

The resulting plot of current versus potential, known as the cyclic voltammogram, provides valuable information about the kinetic aspects of the electron transfer process. In the case of a reversible redox couple, two symmetric peaks are typically observed: one associated with the oxidation and the other with the reduction of the analyte. The midpoint between the anodic and cathodic peak potentials represents the formal potential $E^{0'}$ of the redox couple. The separation between the two peak potentials (ΔE_p) reflects the reversibility of the process, with an ideal Nernstian system displaying a peak-to-peak separation of approximately 59 mV at room temperature for a one electron transfer. The value of the peak current is proportional to the concentration of the electroactive species and to the square root of the scan rate, as described by the Randles–Sevcik equation 2.11.

It is important to note the convention used for plotting cyclic voltammograms. According to the IUPAC recommendation, the x-axis represents the applied potential (increasing from left to right), while the y-axis reports the measured current, with anodic currents considered positive and cathodic currents negative Figure 2.2a. In this study, the IUPAC convention has been consistently followed. As a result, the voltammograms allow the identification of the oxidation and reduction processes occurring at the electrode surface.



(a) Cyclic voltammetry of the reduction of Fc⁺ to Fc following the US convention (opposite to the IUPAC convention adopted in this study).



(b) Evolution of the applied potential with an initial potential E_1 higher than the switching potential E_2 .

Figure 2.2: Cyclic voltammetry illustration showing both the voltammogram (a) and the potential waveform (b). Reprinted from [29]

2.2.2 Differential Pulse Voltammetry

Differential Pulse Voltammetry (DPV) is a refined electrochemical technique that provides superior sensitivity and resolution [31], [32] compared to traditional cyclic voltammetry.

This method operates by imposing a series of small potential pulses of fixed amplitude on a linear potential ramp. At each pulse, two current measurements are taken:the first immediately before the pulse onset, known as the base current (I_{base}) , and the second at the end of the pulse duration, called the pulse current (I_{pulse}) . By calculating the differential current $\Delta I = I_{\text{pulse}} - I_{\text{base}}$, and plotting this against the applied potential, DPV generates voltammograms with sharp and well-defined peaks.

An advantage of DPV is its ability to minimize background capacitive currents. Sampling the current at the end of the pulse suppresses these non Faradaic currents, allowing the Faradaic current that are directly related to the redox reactions of analytes to be detected. This improved signal to noise ratio is essential for detecting low concentrations of electroactive species.

As demonstrated in Figure 2.3, several key parameters govern the DPV measurement and are adjustable via the NOVA software. These parameters include the start and stop potentials that define the scan range, the step potential controlling the increment between successive measurements, modulation amplitude representing the height of each pulse, modulation time specifying the pulse duration, and the interval time between pulses. This waveform and measurement setup ensure precise control over the electrochemical environment and data acquisition timing.

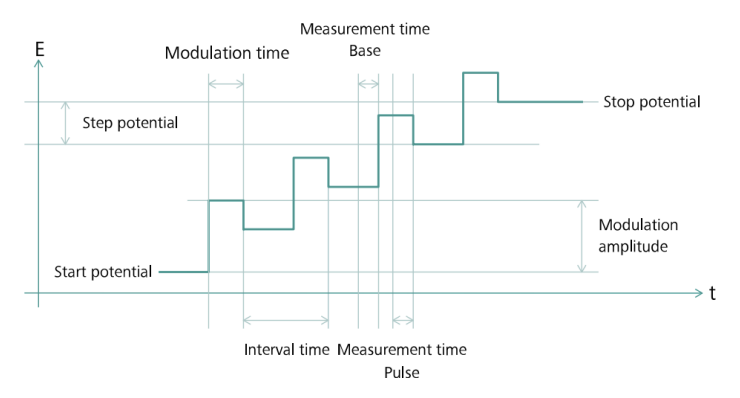


Figure 2.3: Overview of the measurement properties of the Differential Pulse Voltammetry (DPV) command, showing the potential waveform with key parameters such as start potential, stop potential, step potential, modulation amplitude, modulation time, interval time, and measurement times for base and pulse currents. Reprinted from [33]

Electrochemical Impedance Spectroscopy (EIS)

Electrochemical impedance spectroscopy (EIS) is a technique used to investigate the dynamic processes at the electrode/electrolyte interface. The system is perturbed with a small sinusoidal potential over a range of frequencies, and the resulting current is measured. Impedance, defined as the ratio of potential to current, is a complex quantity with a real resistive and an imaginary capacitive component. The frequency dependent analysis of impedance allows discussion of different contributions such as solution resistance, interfacial charge transfer, and double-layer capacitance.

The behavior of the system can be modeled by the Randles equivalent circuit, composed of a solution resistance R_s in series with the parallel combination of charge transfer resistance R_{ct} and double-layer capacitance C_{dl} . The overall impedance $Z(\omega)$ of the Randles circuit is described by the formula:

$$Z(\omega) = R_s + \frac{1}{\frac{1}{R_{ct}} + j\omega C_{dl}}$$

where $j = \sqrt{-1}$ is the imaginary unit and $\omega = 2\pi f$ is the angular frequency of the perturbation.

At high frequencies, the capacitive impedance $\frac{1}{j\omega C_{dl}}$ approaches zero, effectively short circuiting the parallel branch. Thus, the charge transfer resistance R_{ct} becomes negligible, and the measured impedance mainly corresponds to the solution resistance R_s , which represents the ohmic resistance of the electrolyte and cell geometry. Here, the interfacial processes are too slow to respond to the rapid perturbation, so the measured impedance mainly reflects the ohmic resistance of the electrolyte and cell geometry.

At intermediate frequencies, the capacitive reactance is comparable to R_{ct} , and the impedance is dominated by their parallel combination. Here, R_{ct} reflects the kinetics of electron transfer at the electrode interface, a lower R_{ct} indicates faster electron transfer.

The double layer capacitance C_{dl} depends on the electroactive surface area and material properties, representing the electrode's ability to store charge. The frequency-dependent impedance response showing both resistive and capacitive characteristics.

At low frequencies, the capacitive reactance becomes very large, making C_{dl} behave almost like an open circuit. This limits current flow through the capacitive branch, and the impedance is dominated by the charge transfer resistance R_{ct} . In this case the electrode behaves like an ideal capacitor storing charge at the interface. The phase angle of the impedance approaches -90°, and the total impedance magnitude increases, reflecting slow interfacial processes and charge accumulation.

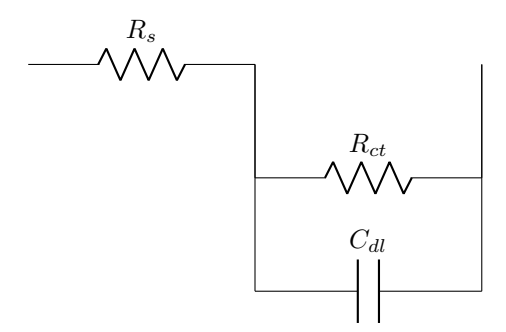


Figure 2.4: Randles equivalent circuit: solution resistance (R_s) in series with the parallel combination of charge transfer resistance (R_{ct}) and double-layer capacitance (C_{dl}) .

2.3 Fundamental Electrochemical Equations

2.3.1 Randles-Sevčík Equation

A crucial parameter in cyclic voltammetry (CV) experiments is the scan rate ν (measured in mV/s), which describes how fast the electrode potential changes over time. The scan rate strongly influences the behavior of the analyte at the working electrode (WE) surface.

Higher scan rates produce a thinner diffusion layer near the electrode, which usually leads to larger peak currents. The peak current i_p depends on the analyte concentration, its diffusion coefficient, and the scan rate. For reversible redox reactions where the species freely diffuse, the Randles-Sevčik equation gives the relationship as:

$$i_p = 0.446 \, nFAc \sqrt{\frac{nF\nu D}{RT}}$$

where n is the number of electrons transferred, F the Faraday constant, A the electrode surface area, c the analyte concentration, D the diffusion coefficient, R the gas constant, and T the temperature in Kelvin.

This equation shows that the peak current i_p is proportional to the square root of the scan rate ν . It is often used to calculate the diffusion coefficient D of the electroactive species.

2.3.2 Laviron Equations

Laviron proposed a set of equations designed to evaluate electron transfer kinetics for systems where diffusion is not the limiting factor, such as when species are adsorbed on the electrode surface [34]. When the product $n\Delta E_p$ (with ΔE_p representing the peak-to-peak separation in volts) exceeds 200 mV, the slopes of the plots of peak potentials versus the logarithm of scan rate $\log \nu$ can be described as follows:

$$m_c = -\frac{2.3RT}{\alpha nF}$$

$$m_a = \frac{2.3RT}{(1-\alpha)nF}$$

Here, m_c and m_a are the slopes for the cathodic (reduction) and anodic (oxidation) peaks respectively, and α is the transfer coefficient indicating the symmetry of the energy barrier for electron transfer.

From these slopes, α can be calculated Equation 2.9:

$$\alpha = \frac{m_a}{m_a - m_c} \tag{2.9}$$

Using the determined α , the electron transfer rate constant k can be found from the equation 2.10:

$$logk = \alpha \log(1 - \alpha) + (1 - \alpha) \log \alpha - \log \left(\frac{RT}{nF\nu}\right) - \frac{\alpha(1 - \alpha)nF\Delta E_p}{2.3RT} \quad (2.10)$$

Laviron's equations also provide methods to determine α and k when $n\Delta E_p$ is less than 200 mV, adapting to cases of slower kinetics or quasi-reversible electron transfers

These relationships are essential for understanding and quantifying electron transfer rates in adsorption-controlled electrochemical systems.

$$i_p = 0.446 \cdot nFAC \cdot \sqrt{\frac{nF\nu D}{RT}}$$
 (2.11)

Equation 2.11 represents the Randles-Sevcik equation, where:

 i_p is the peak current (A)

n is the number of electrons transferred

A is the electrode surface area (cm^2)

C is the concentration of the redox species (mol/cm^3)

D is the diffusion coefficient (cm²/s)

 ν is the scan rate (V/s)

F is the Faraday constant (C/mol)

R is the gas constant $(J/(mol\ K))$

T is the temperature (K)

Chapter 3

Materials and Methods

3.1 Chemicals

All reagents used were purchased from Sigma-Aldrich and employed as received, without any additional purification. For the preparation of europium-based spinels, the nitrate salts of the corresponding metals, copper(II) nitrate trihydrate (Cu(NO₃)₂ · 3H₂O), cobalt(II) nitrate hexahydrate (Co(NO₃)₂ · 6H₂O), zinc(II) nitrate hexahydrate (Zn(NO₃)₂ · 6H₂O), together with europium(III) nitrate hexahydrate were selected as precursors, while urea (CO(NH₂)₂) acted as a fuel and reducing agent in the autocombustion process.

Europium spinel oxide powders were dispersed in butanol $(C_4H_{10}O)$ to prepare the nanomaterial dispersions used for electrode functionalization.

In order to enhance the detection of anticancer drugs, the electrodes were also functionalized with two different isoforms of cytochrome P450: CYP2B6 for cyclophosphamide detection and CYP3A4 for ifosfamide detection. The concentration of the enzyme solutions was $0.5~\mathrm{nM}$, and they were provided by Corning SupersomesTM.

To prepare the electrolyte solutions, ifosfamide (C₇H₁₅Cl₂N₂O₂P · H₂O) and cyclophosphamide (C₇H₁₅Cl₂N₂O₂P · H₂O) were used in both phosphate-buffered saline (PBS) and human serum .

3.2 Synthesis of Europium Oxides

Europium spinel oxides were synthesised by the autocombustion method in the Carbon Group laboratory at the Politecnico di Torino. A schematic of the process followed is shown in Figure 3.1.

For each europium spinel, the metal precursors and urea were mixed in stoichiometric ratios in a crucible to obtain 0.1 g of metal oxide.

The crucible was then heated in a furnace at 600 °C for 1 hour. Afterwards, the metal oxides were collected at room temperature. The yield of the process is summarized in Table 3.1.



Figure 3.1: Schematic representation of the autocombustion synthesis method for europium spinel oxides.

Material	Yield (%)
$ZnEu_2O_4$	88.6
$CuEu_2O_4$	91.5
$CoEu_2O_4$	90.2

Table 3.1: Yield of europium spinel oxides.

3.3 Electrode Functionalization

Electrode functionalization and performance testing were carried out at the Bio/CMOS Interfaces group at the École Polytechnique Fédérale de Lausanne (EPFL), Switzerland.

3.3.1 Functionalization with Europium Spinel Oxides

Electrochemical characterization was performed using single working electrode sensors (DRP-11L). These sensors have a single carbon working electrode of 0.40 cm diameter, with an active area of approximately 0.12 cm².

For electrode modification, europium oxide powders were ground into a fine powder using a mortar. Suspensions were prepared by dispersing 3 mg of europium based spinel oxide powder in 1 mL of butanol and sonicated for 30 minutes to obtain homogeneity. A volume of 5 μ L of the suspension was drop-cast on the working electrode surface and dried overnight at room temperature to immobilize the material on the electrode [35]. Three independent electrodes were prepared for each europium oxide material to ensure reproducibility.

3.3.2 Functionalization with Europium Spinel Oxides and Cytochrome P450 Enzymes

For biosensing experiments, europium oxide-modified dual sensors (DRP-X1110) with two working electrodes were used. One working electrode was modified exclusively with europium oxide material following the same procedures as the

single sensors, while the other electrode was further functionalized the enzymes. The enzymes chosen for functionalization are two cytochrome P450 isoforms, CYP2B6 and CYP3A4, due to their roles in metabolizing cyclophosphamide and ifosfamide, respectively.

Enzyme solutions (3 μ L) were applied via drop-casting onto the electrode surface and stored overnight at 4 °C to facilitate enzyme binding with the europium oxide nanoparticles.

A schematic illustrating the dual sensor configuration is shown in Figure 3.2.

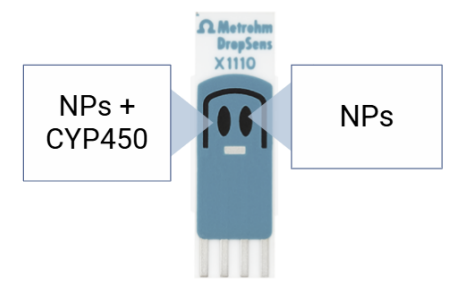


Figure 3.2: Schematic illustration of the dual sensor setup. The right working electrode is modified with europium oxide nanoparticles only, while the left working electrode is modified with europium oxide nanoparticles functionalized with cytochrome P450 enzyme.

3.4 Materials Characterization

3.4.1 Crystal Structure Analysis

X-ray diffraction (XRD) analysis was carried out to examine the crystalline structure and phase composition of the synthesized europium oxides nanomaterials. A copper (Cu) X-ray source was used during the measurements. The obtained diffraction patterns were analyzed using the software *QualIX* to identify the crystal phases and evaluate the material's structural properties.

The XRD pattern typically shows well defined peaks at specific diffraction angles corresponding to the crystal planes of the material. These peaks indicate the crystalline nature of the europium oxide nanoparticles and allow the determination of lattice parameters and phase purity. The intensity and position of the peaks provide information on the crystallite size and the presence of any secondary phases or impurities.

Raman spectroscopy is a non destructive analytical technique used to study the surface properties of materials. It provides detailed about the chemical composition, phase, crystallinity, environmental conditions, and molecular interactions within a sample. This method involves illuminating the sample with a high intensity laser, which interacts with the molecular vibrations of the material. As a result, the scattered light shifts to different wavelengths compared to the original laser source and this shift is characteristic of the chemical bonds present in the sample.

The final output is a Raman spectrum, displaying peaks at various wavelengths and intensities corresponding to different vibrational modes, effectively acting as a unique molecular fingerprint of the analyzed material [36]. In this work, the samples were examined using a Renishaw Raman Microscope, equipped with a 785 nm infrared laser set at 0.5 mW power.

3.4.2 Morphological Analysis

Field-Emission Scanning Electron Microscopy (FESEM) is a technique employed to study the surface morphology and microstructural features of nanomaterials with high spatial resolution.

In this method, a focused electron beam is scanned over the sample surface, causing the emission of secondary electrons due to electron powder interactions. These emitted electrons are collected to generate images revealing the topography and surface characteristics of the material at the nanoscale [37].

In this research, FESEM analyses were conducted using a Zeiss Supra 40 microscope (Oberkochen, Germany) to characterize the morphology of the synthesized nanomaterials and to assess the surface uniformity of europium oxides functionalization on the electrodes.

The electron beam energy was maintained at 5 keV and to enhance the conductivity of the samples and improve image contrast, a thin platinum layer was sputtered on top of the surfaces before the analysis.

3.5 Preparation of Electrolytic Solutions

3.5.1 PBS Solution

The electrolyte solution used was a 0.1 M phosphate-buffered saline (PBS) with a pH of 7.4 at 25 °C. Thanks to its buffering capacity, this solution ensures compatibility with biological samples and maintains stable conditions for electrochemical measurements.

3.5.2 Ferro/Ferricanide Solution

For the preparation of the ferro/ferricyanide redox probe solution, 42.24 mg of potassium hexacyanoferrate(II) trihydrate and 32.92 mg of potassium hexacyanoferrate(III) were weighed using a microbalance. These compounds were then dissolved and mixed in 50 mL of previously prepared phosphate-buffered saline (PBS) solution to obtain a homogeneous redox probe for electrochemical characterization.

3.5.3 Cyclophosphamide and Ifosfamide Solution

Cyclophosphamide solutions were prepared at various concentrations from 5 μ M to 100 μ M, chosen based on doses reported for the rapeutic efficacy. [38],[39] To prepare these solutions, first a 1 mM stock solution was made by weighing 2.79 mg of cyclophosphamide and dissolving it in 10 mL of phosphate buffered saline (PBS). Then dilutions of the stock solution were performed to have the target concentrations as illustretes in Table 3.2. All dilutions were made to have a final volume of 2 mL.

Ifosfamide solutions were prepared as cyclophosphamide ones but in a different pharmacologically relevant concentration range, from 10 μ M to 120 μ M. The stock solution, made by dissolving 2.61 mg of ifosfamide in 10 mL PBS, all the dilutions are detailed in the Table 3.3.

All solutions were stored at 4 °C to maintain stability.

Table 3.2: Volumes of 1 mM cyclophosphamide stock solution and PBS required to prepare target concentrations ranging from 5 to 100 μ M

Target Concentration (μM)	Stock Volume (μL)	PBS Volume (μL)
5	10	1990
10	20	1980
25	50	1950
50	100	1900
75	150	1850
100	200	1800

Table 3.3: Volumes of 1 mM ifosfamide stock solution and PBS required to prepare target concentrations ranging from 10 to 120 μ M

Target Concentration (μM)	Stock Volume (μL)	PBS Volume (μ L)
10	20	1980
20	40	1960
40	80	1920
60	120	1880
80	160	1840
100	200	1800
120	240	1760

3.6 Electrochemical Measurements

Electrochemical measurements were conducted using the AUT302N.MBA potentiostat connected to the electrode under analysis and to a computer for real-time data acquisition through NOVA software.

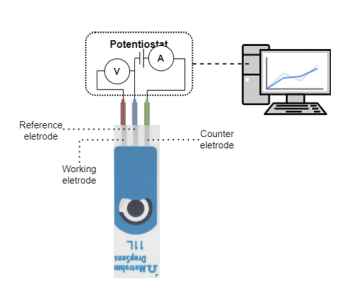
A schematic of the general measurement setup is shown in Figure 3.3a.

The electrochemical techniques performed were cyclic voltammetry (CV), differential pulse voltammetry (DPV), and electrochemical impedance spectroscopy (EIS).

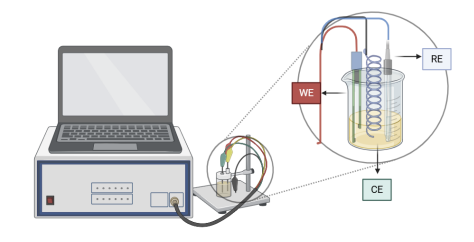
3.6.1 Ferro/Ferricyanide Characterization

The europium oxides nanomaterials were first characterized in ferro/ferricyanide electrolyte solution using SPE 11L Metrohm single electrodes because the ferro/ferricyanide redox couple is a reversible system known for well defined redox peaks in cyclic voltammetry.

Cyclic voltammetry (CV) and electrochemical impedance spectroscopy (EIS) were carried out in a dipping configuration as shown in Figure 3.3b to have a stable conditions.



(a) Schematic of the general electrochemical measurement setup using AUT302N.MBA potentiostat.



(b) Schematic representation of the dipping configuration screen-printed working electrode (WE), platinum wire counter electrode (CE), and external Ag/AgCl reference electrode (RE).

Figure 3.3: Electrochemical measurement setups: (a) general AUT302N.MBA potentiostat configuration, and (b) dipping configuration with SPCE, CE, and RE.

Three cyclic voltammetry (CV) scans were performed at each scan rate, ranging from 25 to 150 mV/s in increments of 25 mV/s. This was repeated for three electrodes of each material.

Electrochemical parameters were calculated from the cyclic voltammetry data. The relative electroactive surface area was estimated as the ratio between the slope of the anodic peak current (I_{pa}) versus the square root of the scan rate $(\sqrt{\nu})$ for the modified material and that of the bare electrode.

The diffusion coefficient D was determined according to the Randles-Sevcik equation (2.11) considering n=1 the number of electrons transferred, A is the electroactive surface area of the electrode 0.12 cm², $C=2\times10^{-6}$ mol/cm³ is the concentration of the ferro/ferricyanide used.

The electron transfer coefficient α was calculated using Laviron's (2.9). And the electron transfer rate constant k_s was calculated using the equation (2.10), considering the peak potential separation ΔE_p at a scan rate of 100 mV/s.

Electrochemical impedance spectroscopy (EIS) measurements were performed to characterize the modified electrodes.

The measurements were carried out using a potentiostat connected as shown in Figure 3.3a equipped with a Frequency Response Analyzer (FRA) module.

A small sinusoidal AC voltage (10 mV $_{\rm RMS}$) was applied at the open circuit potential (OCP), while the impedance response of the system was recorded over a wide frequency range. The frequency was swept in logarithmic steps from 100 kHz to 0.1 Hz. In this study, the analysis was limited to a qualitative comparison of Bode magnitude and phase plots between bare sensors and sensors modified with metal oxide nanoparticles. This comparison allowed the evaluation of changes in the electrochemical behavior induced by the nanoparticle modification without performing a full equivalent circuit fitting.

The specific parameters used for the EIS measurements are summarized in Table 3.4.

Parameter	Value	Unit / Description
First applied frequency	1.0×10^{5}	Hz
Last applied frequency	0.1	Hz
Number of frequencies	10	Points per decade

Table 3.4: Experimental parameters for EIS measurements

3.6.2 Cyclophosphamide and Ifosfamide Measurements

For cyclophosphamide and ifosfamide detection cyclic voltammetry (CV) and deep pulse voltammetry (DPV) were performed and the parameters set are in the Table 3.5 and 3.6 . The measurements were performed using the configuration shown in Figure 3.3a, where 100 \upmu L droplets of analyte solution were deposited on dual screen-printed electrodes , covering the two working, reference, and counter electrodes.

For each material, three different electrodes were tested. Each electrode was cleaned by performing 5 cyclic voltammetry scans in PBS, and rinsed and air aried between measurements. Then, three scans were performed at different concentrations show in the Table 3.7 selected based on the pharmacological range of the drug.

Differential Pulse Voltammetry (DPV) Parameters		
Parameter	Value	
Start potential	0.4 V (vs REF)	
Stop potential	-0.6 V (vs REF)	
Step	-0.005 V	
Modulation amplitude	0.1 V	
Modulation time	$0.05 \mathrm{\ s}$	
Interval time	$0.5 \mathrm{\ s}$	

Table 3.5: DPV parameters used for cyclophosphamide and ifosfamide measurements.

Cyclic Voltammetry	(CV) Parameters
Parameter	Value
Start potential	-0.6 V (vs REF)
Upper vertex potential	$+0.4 \mathrm{~V~(vs~REF)}$
Lower vertex potential	-0.6 V (vs REF)
Number of scans	3
Scan rate	$0.02~\mathrm{V/s}$

Table 3.6: CV parameters used for cyclophosphamide and ifosfamide measurements.

Analyte	Concentration Range (µM)
Cyclophosphamide	5, 10, 25, 50, 75, 100
Ifosfamide	10, 20, 40, 60, 80, 100, 120

Table 3.7: Concentration ranges for cyclophosphamide and ifosfamide used in droplet configuration measurements.

After baseline subtraction, the DPV oxidation peak currents were inverted from negative values to positive. The maximum peak currents were then extracted and plotted against the drug concentrations to obtain the calibration curves for each europium-based spinel oxide. For each material, measurements were perform the sensitivity (S), coefficient of determination (R^2) , and limit of detection (LoD) were calculated by averaging the data across these electrodes.

The slope of the linear regression of the averaged data points provided the sensitivity (S), and the coefficient of determination (R²) confirmed the linearity of the sensor response over the tested range.

The limit of detection (LoD) was calculated according to Equation (3.1)

$$LoD = k \cdot \frac{\sigma}{S} \tag{3.1}$$

where k=3 corresponds to a 99.7% confidence level in distinguishing the signal from noise, and σ is the standard deviation of the blank (only PBS) [40].

Chapter 4

Results and Discussion

4.1 Material Characterization

4.1.1 Crystal Structure Analysis (XRD and Raman)

The XRD data for the synthesized samples were obtained from the original .qlx files, followed by baseline subtraction and noise filtering to enhance data quality. The structural analysis was carried out on three europium-based spinel oxides: $ZnEu_2O_4$, $CuEu_2O_4$, and $CoEu_2O_4$. To evaluate the phase composition and crystallinity, the diffraction patterns were compared against literature data and reference oxides.

In the case of CuEu_2O_4 , the XRD pattern (Figure 4.1) exhibits several peaks at approximately $2\theta = 24^\circ$, 32.2° , 32.8° , 46.5° , 47.2° , 57.1° , and 57.6° . These peaks correspond well to the characteristic lattice planes of the CuEu_2O_4 spinel structure reported in the literature [41], confirming the successful synthesis of this phase with high crystallinity. In addition , there is a minor additional peak near $2\theta \approx 28^\circ$ suggests the presence of a small amount of Eu_3O_4 impurity [42], which is absent in the reference pattern. This indicates that while the primary phase is well-formed CuEu_2O_4 , a secondary phase may coexist in trace amounts (Figure 4.1).

For the $\rm ZnEu_2O_4$ sample, the XRD pattern shows main diffraction peaks at approximately 28.5°, 36°, 42.8°, 56.5°, and 62.1°. These match the characteristic (220), (311), (400), (511), and (440) planes of a cubic spinel lattice similar to $\rm ZnFe_2O_4$ [43], indicating that the dominant crystalline phase in the material is a spinel type structure. However, additional peaks detected at 31.9° and 36.3° can be indexed to the (100) and (101) planes of $\rm ZnO$ [44], revealing the presence of $\rm ZnO$ as a secondary phase. Moreover, a peak at 32.9° corresponds to $\rm Eu_2O_3$ [42], from partial segregation or incomplete incorporation of europium during synthesis. These observations confirm that while $\rm ZnEu_2O_4$ is the main phase, minor oxide impurities coexist (Figure 4.2).

Similarly, the $CoEu_2O_4$ diffraction pattern exhibits main peaks near 28° , 37° , 42° , 47° , 59° , and 61° , consistent with the ones characteristic of the spinel

structure and comparable to the reference $CoFe_2O_4$ spectrum [45]. Some peaks, particularly those around 37° and 42°, suggest the presence of CoO as a secondary phase [46].

Additionally, weak peaks between $29^{\circ}-35^{\circ}$ and $50^{\circ}-56^{\circ}$ hint at minor Eu₂O₃ impurity, a typical secondary phase in these spinel materials [42](Figure 4.3).

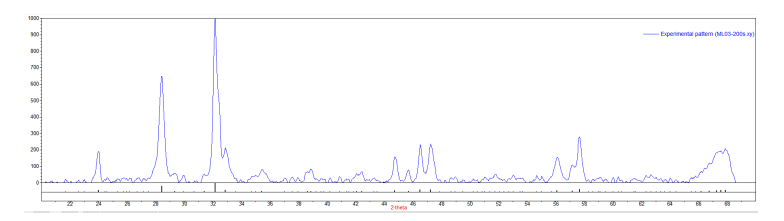


Figure 4.1: XRD pattern of the $CuEu_2O_4$ sample showing characteristic spinel reflections and minor Eu_3O_4 impurity.

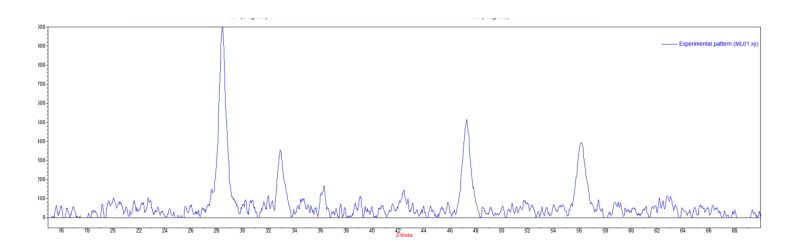


Figure 4.2: XRD pattern of the $\rm ZnEu_2O_4$ sample with major spinel peaks and secondary phases ZnO and $\rm Eu_2O_3$.

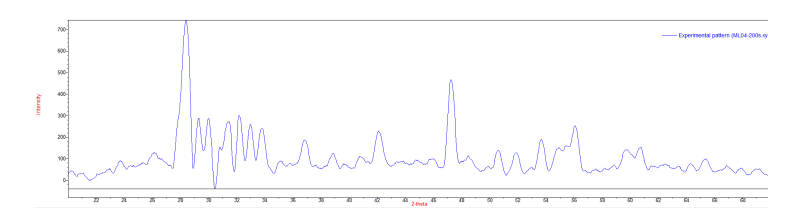


Figure 4.3: XRD pattern of the $CoEu_2O_4$ sample indicating spinel phase with CoO and Eu_2O_3 impurities.

Raman spectroscopy was employed to further characterize the samples, with spectra processed from .txt files using Origin software.

Baseline subtraction was applied to reduce background noise. Due to limited Raman reference data for europium spinels in the literature, analysis focused mainly on comparing the three samples to identify characteristic vibrational modes and confirm their composition.

The ${\rm CuEu_2O_4}$ Raman spectrum shows a prominent peak around 150 cm⁻¹, attributed to the ${\rm T_{2g}}(1)$ mode of ${\rm CuFe_2O_4}$ [[47]]. Additional peaks between

200 and 300 cm⁻¹ correspond to A_g and B_g modes, likely indicative of CuO impurities [48], while a peak near 400 cm⁻¹ suggests the presence of Eu₂O₃ [42]. Higher wavenumber features around 700 cm⁻¹ are assigned to the $A_{1g}(1)$ mode of CuFe₂O₄ (Figure 4.4).

In the $CoEu_2O_4$ sample, the Raman spectrum exhibits a peak near 250 cm⁻¹ matching the $T_{2g}(3)$ mode of $CoFe_2O_4$ [49], with an additional 400 cm⁻¹ peak indicative of Eu_2O_3 [42]. Peaks near 600 and 700 cm⁻¹ are associated with the $A_{1g}(2)$ and $A_{1g}(1)$ vibrational modes of $CoFe_2O_4$, respectively (Figure 4.5).

The ZnEu_2O_4 spectrum features a peak around 190 cm⁻¹ corresponding to the $\text{T}_{2g}(1)$ mode of ZnFe_2O_4 [50], another peak near 330 cm⁻¹ assigned to the $\text{T}_{2g}(2)$ mode, and a peak at approximately 650 cm⁻¹ for the $\text{A}_{1g}(1)$ mode of ZnFe_2O_4 . A low-frequency peak near 90 cm⁻¹ is attributed to ZnO [44], supporting the secondary phase presence revealed by XRD (Figure ??).

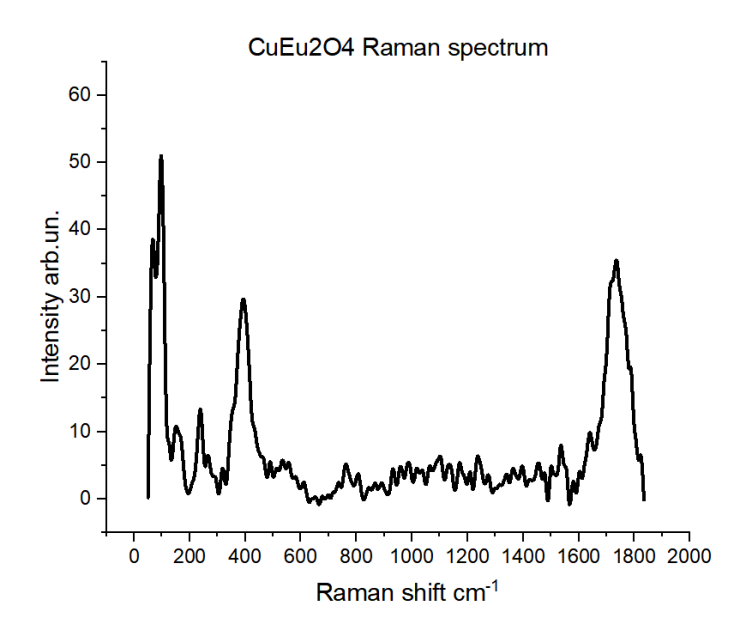


Figure 4.4: Raman spectrum of the ${\rm CuEu_2O_4}$ sample showing characteristic vibrational modes and impurity contributions.

Overall, the combined XRD and Raman analyses confirm that the synthesized materials form europium based spinel oxides with good crystallinity, while minor secondary impurity phases such as Eu_2O_3 and metal oxides (ZnO, CuO, CoO) coexist in low amounts.

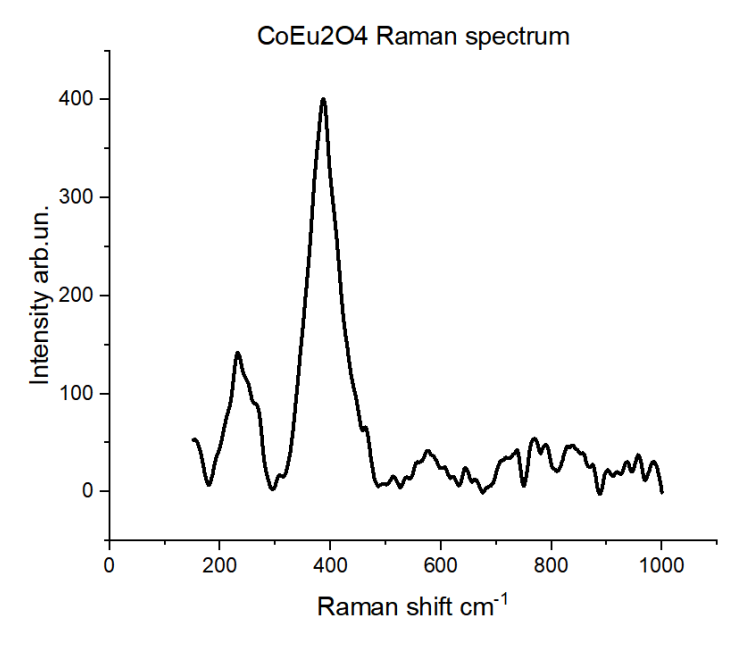


Figure 4.5: Raman spectrum of the $CoEu_2O_4$ sample indicating major vibrational modes and minor Eu_2O_3 impurity.

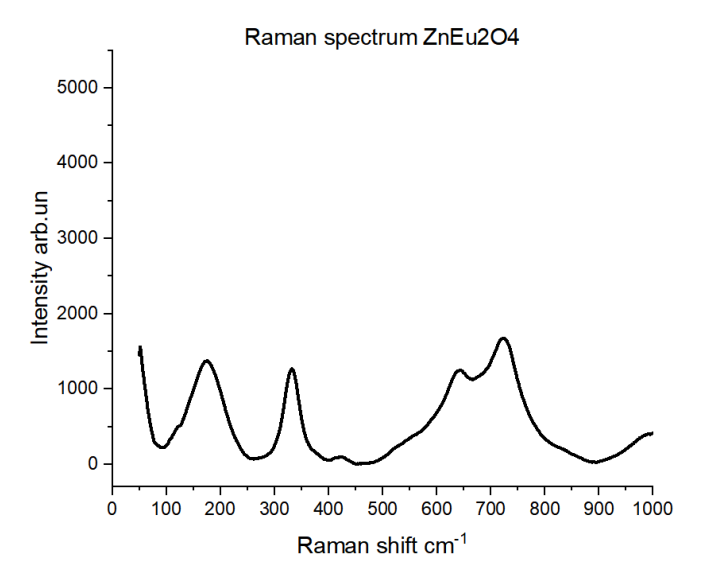


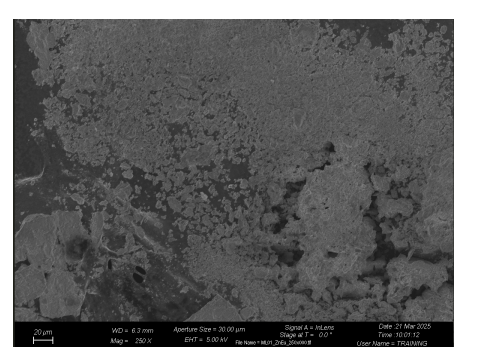
Figure 4.6: Raman spectrum of the $\rm ZnEu_2O_4$ sample with spinel vibrational modes and ZnO secondary phase.

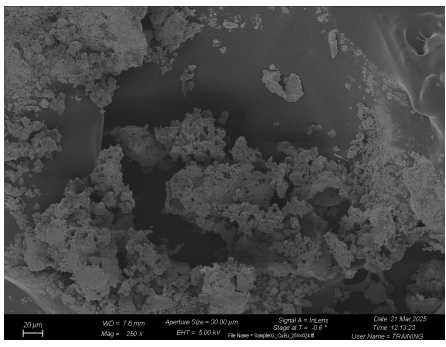
4.1.2 Morphological Analysis (FESEM)

To study the morphology of the synthesised europium spinel oxide the morphological analysis FESEM weas carried out.

The FESEM images of ZnEu₂O₄, CuEu₂O₄, and CoEu₂O₄ nanoparticles are shown in Figures 4.7a, 4.7b, and 4.7c.

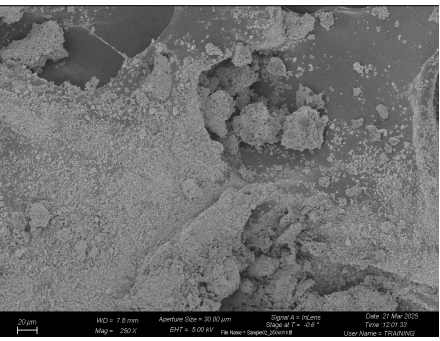
The images show that the nanoparticles display a regular morphology and their average size is around $100~\rm nm$.





(a) $ZnEu_2O_4$ nanoparticles (scale bar = $20 \mu m$).

(b) CuEu₂O₄ nanoparticles (scale bar = 20 $\mu m).$



(c) $CoEu_2O_4$ nanoparticles (scale bar = $20 \mu m$).

Figure 4.7: FESEM images of europium-based spinel oxide nanoparticles

4.2 Electrochemical Characterization in Ferro/Ferricyanide

4.2.1 Cyclic Voltammetry (CV) Analysis and Kinetic Parameter Calculation

Electrochemical characterization of single electrodes modified with europium oxide materials $\rm ZnEu_2O_4,\, CuEu_2O_4,\, and\, CoEu_2O_4$ was conducted using cyclic

voltammetry (CV) in dipping configuration, as described in the Methods section, with the setup shown in Figure 3.3b.

After initial cleaning in phosphate-buffered saline , for each scan rate from 25mV/s to 150 mV/s five scans were recorded, discarding the first two due to signal instability. The last three scans were averaged to consider intra-electrode variability. Also, three independently prepared electrodes were tested for each material to assess inter-electrode variability. Results are presented as mean \pm estimated standard deviation.

The cyclic voltammograms obtained, as shown in Figures 4.8a to 4.8j, exhibit characteristic symmetrical redox peaks typical of the ferro/ferricyanide redox couple, demonstrating a reversible transfer process controlled by diffusion.

Both anodic (I_{pa}) and cathodic (I_{pc}) peak currents increase linearly with the square root of the scan rate (ν), in agreement with the Randles-Sevcik equation (2.11), confirming diffusion-controlled kinetics.

Table 4.1 summarizes the linear regression parameters of peak currents versus $\sqrt{\nu}$, it shows that among modified electrodes, CuEu₂O₄ presents the highest slope values (I_{pa}: 9.65 μ A/ $\sqrt{mV/s}$, I_{pc}: -5.92 μ A/ $\sqrt{mV/s}$), followed by CoEu₂O₄ and ZnEu₂O₄, confirming an increased electroactive surface area, also reflected in the relative area values shown in Table 4.3.

The peak potentials (E_{pa} and E_{pc}) plotted versus the natural logarithm of the scan rate ($\ln \nu$) were calculated and reported in Table 4.2.

The ZnEu₂O₄ shows ΔE_p values closer to the bare electrode indicative of more reversible kinetics, while CuEu₂O₄ and CoEu₂O₄ exhibit larger values (>500 mV), suggesting slower and less reversible electron transfer processes.

All kinetic parameters, including the charge transfer coefficient α , the diffusion coefficient D, the kinetic rate constant k_s and the relative electroactive surface areas, were evaluated for all electrodes and summarized in Table 4.3.

The charge transfer coefficient α is near 0.5 for bare and ZnEu₂O₄ electrodes, confirming near-symmetrical energy barriers.CuEu₂O₄ and CoEu₂O₄ present lower α values, consistent with their larger ΔE_p and slower kinetics.

The diffusion coefficients are highest for CuEu_2O_4 and CoEu_2O_4 , enhancing mass transport, it reflects how fast the electroactive species move through the solution towards the electrode surface, thus directly impacting mass transport. Typically, a higher diffusion coefficient is associated with a larger effective electroactive surface area, which facilitates the arrival of more reactant molecules at the electrode. This is observed for CuEu_2O_4 and CoEu_2O_4 , where D is higher, and the relative electroactive areas are also larger (relative areas 2.34 and 1.57 respectively), enhancing mass transport and current response.

However, the electron transfer kinetics, indicated by the kinetic rate constant k_s , represent how rapidly the electrons are exchanged between the electrode and the electroactive species at the interface.

 ${\rm ZnEu_2O_4}$, despite having a diffusion coefficient and electroactive area comparable to the bare electrode, shows a significantly higher k_s , indicating faster electron transfer rates.

This reveals an important balance: increasing the electroactive surface area

and diffusion coefficient can enhance mass transport, but it does not necessarily improve the electron transfer kinetics, which depend on the intrinsic properties of the electrode material and its interface with the electrolyte.

Table 4.1: Linear regression of peak currents vs. $\sqrt{\nu}$.

Material	Slope $I_{pa} (\mu A/\sqrt{mV/s})$	$R^2 I_{pa}$	Slope $I_{pc} (\mu A/\sqrt{mV/s})$	$R^2 I_{pc}$
Bare	4.1 ± 0.53	1.00 ± 0.01	3.3 ± 0.34	1.00 ± 0.01
${\rm ZnEu_2O_4}$	4.0 ± 0.61	0.99 ± 0.01	-3.2 ± 0.55	1.00 ± 0.00
$CuEu_2O_4$	9.7 ± 3.5	0.99 ± 0.01	-5.9 ± 0.27	0.99 ± 0.02
$CoEu_2O_4$	6.5 ± 0.60	0.93 ± 0.04	-5.1 ± 0.41	0.91 ± 0.11

Table 4.2: Linear regression of peak potentials vs. $\ln \nu$ and potential difference ΔE_p .

Material	Slope E_{pa} (mV)	$R^2 E_{pa}$	Slope E_{pc} (mV)	$R^2 E_{pc}$	$\Delta E_p \; (\text{mV})$
Bare	38 ± 12	0.96 ± 0.04	-30 ± 32	0.97 ± 0.02	247 ± 15
${\rm ZnEu_2O_4}$	64 ± 14	0.95 ± 0.06	-59 ± 24	0.95 ± 0.03	332 ± 46
$CuEu_2O_4$	112 ± 20	0.75 ± 0.32	-144 ± 74	0.82 ± 0.22	570 ± 122
$CoEu_2O_4$	107 ± 37	0.91 ± 0.06	-111 ± 18	0.86 ± 0.12	514 ± 46

Table 4.3: Summary of kinetic parameters and relative electroactive surface area.

Material	α	$\mathrm{D}\;(\mathrm{cm}^2/\mathrm{s})$	$k_s \; ({\rm s}^{-1})$	Relative Area
Bare	0.56 ± 0.05	$(1.87 \pm 0.45) \times 10^{-7}$	0.046 ± 0.009	reference
$\rm ZnEu_2O_4$	0.53 ± 0.04	$(2.25 \pm 0.7) \times 10^{-7}$	0.083 ± 0.032	0.98 ± 0.15
$CuEu_2O_4$	0.46 ± 0.16	$(1.37 \pm 1.02) \times 10^{-6}$	0.015 ± 0.017	2.34 ± 0.85
$CoEu_2O_4$	0.48 ± 0.06	$(5.75 \pm 0.1) \times 10^{-7}$	0.015 ± 0.006	1.57 ± 0.15

Electrochemical impedance spectroscopy (EIS) was carried out in a ferro/ferricyanide solution to evaluate the interfacial properties of the bare electrode and the europium-based spinel-modified electrodes (ZnEu_2O_4 , CoEu_2O_4 , and CuEu_2O_4). The data are presented as Bode plots, showing both the impedance modulus (|Z| vs. $\log f$) and the phase angle (° vs. $\log f$). As shown in Figure 4.9a, the bare electrode exhibits the highest impedance magnitude (|Z|) across the entire frequency range, particularly in the low-frequency region, reflecting a slow electron transfer kinetics typical of an unmodified carbon surface in the ferro/ferricyanide redox system. The phase angle of the bare electrode remains relatively low, indicating limited capacitive behavior and poor interfacial activity.

In contrast, all europium-based spinel-modified electrodes demonstrate significantly lower impedance magnitudes, especially at low frequencies, indicative of enhanced charge transfer kinetics as shown in Figure 4.9b-d. Among them, ${\rm CuEu_2O_4}$ displays the lowest |Z| values, revealing the most efficient electron transfer process. ${\rm CoEu_2O_4}$ shows moderately reduced impedance compared to the bare electrode, while ${\rm ZnEu_2O_4}$ maintains the highest impedance among the modified samples, suggesting slower kinetics relative to the others.

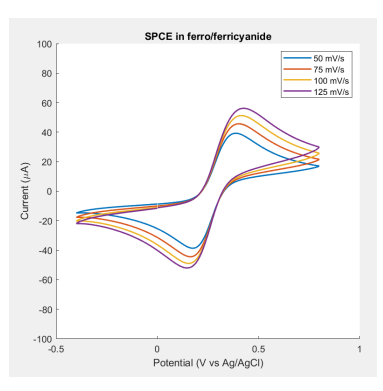
The phase plots show similar findings. Modified electrodes exhibit a more distinct phase maximum in the intermediate frequency range, with phase angles varying from approximately -70° to -20° , which correlate with capacitive double-layer charging process. This phase peak is less pronounced in the bare electrode, further indicating its limited interfacial electrochemical activity.

Overall, these EIS results demonstrate the clear improvement in interfacial properties and enhance of the electrochemical response thanks to europium-based spinel modifications, with CuEu_2O_4 showing the superior electrochemical performance, followed by CoEu_2O_4 and then ZnEu_2O_4 , consistent with the trends observed in the Bode plots.

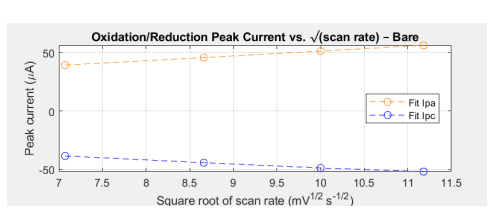
As summarized in Table 4.4, the three nanoparticulate oxide materials exhibit distinct electrochemical characteristics.

Table 4.4: Summary of electrochemical characteristics of the materials.

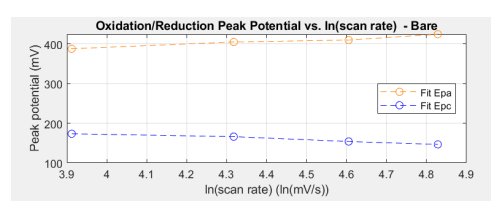
Material	Summary of Electrochemical Characteristics
$\overline{\mathrm{ZnEu_2O_4}}$	Exhibits peak currents similar to the bare electrode, indicating compara-
	ble electrochemical activity. The redox process is diffusion-controlled and
	reversible, with balanced electron transfer kinetics and moderate peak
	potential separation.
$CuEu_2O_4$	Shows significantly higher peak currents attributed to a larger electroac-
	tive surface area, but a higher peak potential separation (ΔE_p) indicates
	slower and less reversible electron transfer kinetics, despite enhanced
	mass transport.
$CoEu_2O_4$	Similar to CuEu ₂ O ₄ with enhanced peak currents and electroactive area,
	but kinetics are slower and reversibility is reduced compared to ${\rm ZnEu_2O_4}.$



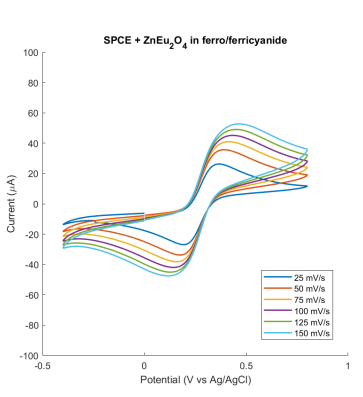
(a) CV bare electrode recorded at scan rates ranging from 25 to 150 $\,$ mV/s



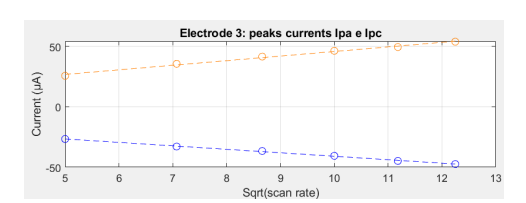
(b) Oxidation (orange) and reduction (blue) currents vs $\sqrt{\nu}$



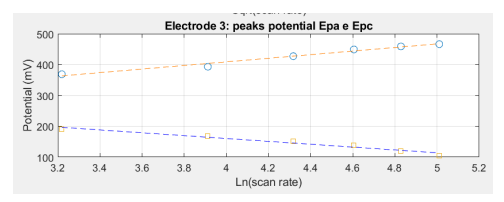
(c) Oxidation (orange) and reduction (blue) potentials vs $\ln(\nu)$



(d) CV ZnEu $_2$ O $_4$ electrode recorded at scan rates ranging from 25 to 150 mV/s

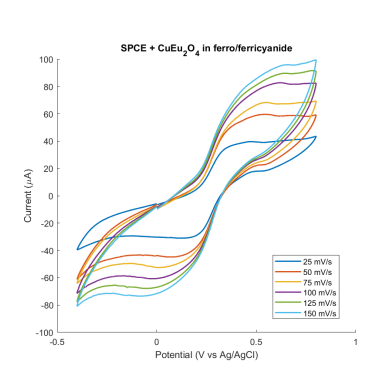


(e) Oxidation (orange) and reduction (blue) currents vs $\sqrt{\nu}$

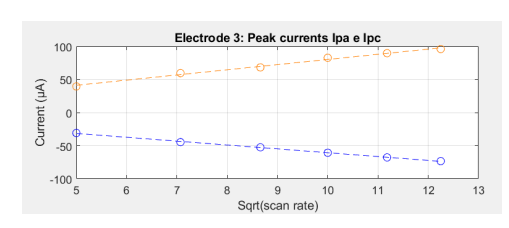


(f) Oxidation (orange) and reduction (blue) potentials vs $\ln(\nu)$

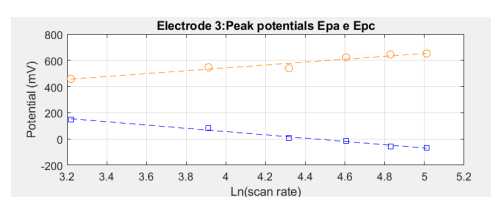
Figure 4.8: Elettrochemical characterization in ferro/ferriciany de: bare electrode e $\rm ZnEu_2O_4.$



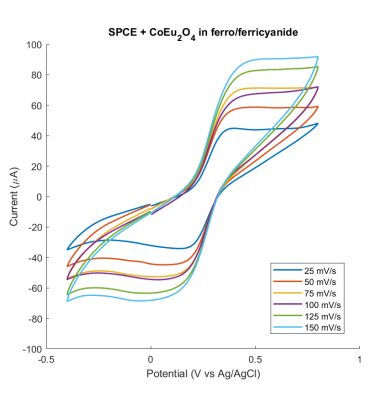
(g) CV $CuEu_2O_4$ electrode recorded at scan rates ranging from 25 to 150 mV/s



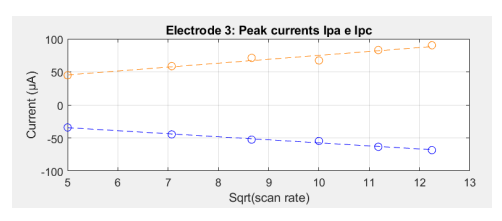
(h) Oxidation (orange) and reduction (blue) currents vs $\sqrt{\nu}$



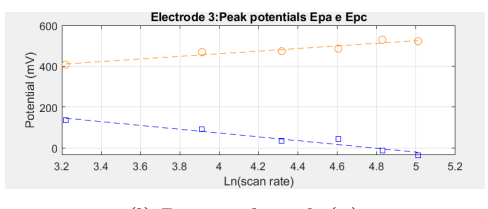
(i) Oxidation (orange) and reduction (blue) potentials vs $\ln(\nu)$



(j) CV CoEu $_2$ O $_4$ electrode recorded at scan rates ranging from 25 to 150 mV/s



(k) Currents vs $\sqrt{\nu}$



(l) Potentials vs $\ln(\nu)$

Figure 4.8: Elettrochemical characterization in ferro/ferriciany de ${\rm CuEu_2O_4}$ e ${\rm CoEu_2O_4}.$

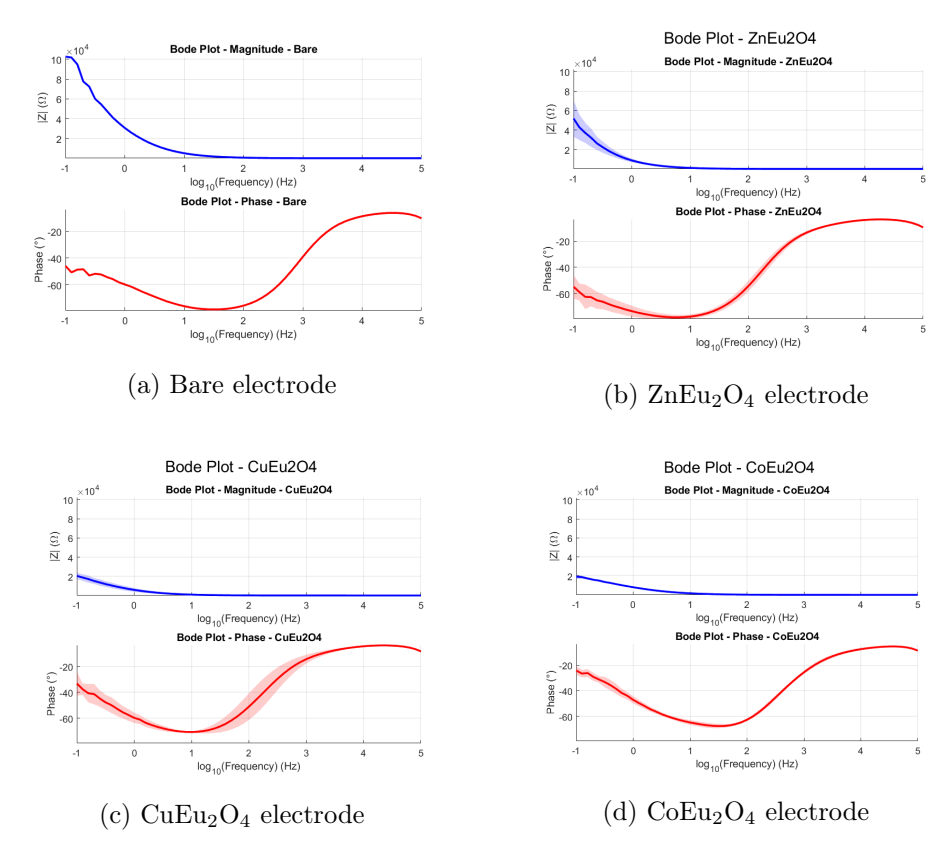


Figure 4.9: EIS Bode plots of the electrodes in a ferro/ferricyanide solution; three-electrode configuration for all materials except the bare electrode.

4.2.2 Cyclophosphamide and Ifosfamide detection without enzymes

As already mentioned, dual electrodes were used with the setup shown in Figure 3.3a for cyclophosphamide and ifosfamide detection. First, the data from the working electrode without enzyme were analyzed, where the electrochemical response reflects only the interaction between the drug and the electrode surface. The cyclic voltammetry performed did not display well defined redox peaks and the recorded currents were close to the background level. Similar results were observed for ifosfamide.

The two drugs cannot be measured, highlighting the necessity of an enzymatic layer to selectively detect the drugs.

4.2.3 Cyclophosphamide Detection with CYP2B6

Dual electrodes modified with europium oxides and CYP2B6 enabled the electrochemical detection of cyclophosphamide.

In both cyclic voltammetry (CV) and differential pulse voltammetry (DPV), an enzymatic peak was observed around -400 mV, reflecting the activity of cytochrome P450 which is consistent with previously reported values in the literature [25].

However, in the CVs the peak currents remained similar across the tested range,instead the DPV provided a clearer and more sensitive response, where the cathodic peak at approximately –400 mV became progressively higher as the cyclophosphamide concentration increased.

After baseline subtraction and inversion of negative peaks the calibration curves were obtained.

Three calibrations were performed using three different electrodes for each material, and the curves presented represent the mean values with their corresponding standard deviations in Figure 4.10.

For the CoEu_2O_4 material, the calibration curve was evaluated up to 50 μM , since at higher concentrations the sensor response showed saturation. Therefore, the calibration was limited to this range to ensure accurate sensitivity .

Table 4.5 summarizes the sensitivity, R^2 , and limit of detection (LoD) values calculated for each material with the equation (3.1).

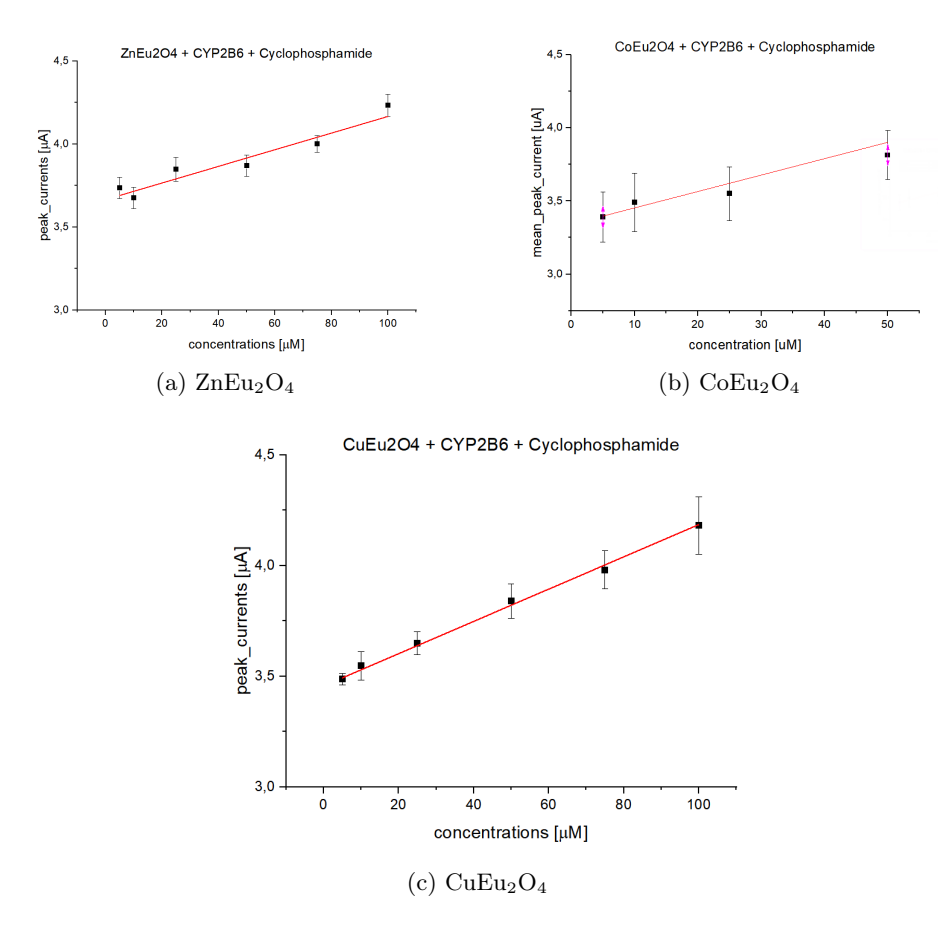


Figure 4.10: Calibration curves for the three europium spinel oxide materials: (a) $\rm ZnEu_2O_4$, (b) $\rm CoEu_2O_4$, and (c) $\rm CuEu_2O_4$ with CYP2B6 enzymes for cyclophosphamide detection.

Material + CYP2B6	$\begin{array}{c} \textbf{Slope} \\ (\mu \textbf{A}/\mu \textbf{M}) \end{array}$	$egin{aligned} ext{Relative} \ ext{Sensitivity} \ ext{(nA/(μM·mm}^2$))} \end{aligned}$	R-Square	$\mathbf{LOD} \\ (\mu \mathbf{M})$
$ZnEu_2O_4$	0.005 ± 0.0007	0.94 ± 0.13	0.93	23.8 ± 0.6
$CoEu_2O_4$	0.011 ± 0.23	2.10 ± 0.23	0.98	17.5 ± 1.5
$CuEu_2O_4$	0.007 ± 0.0002	1.37 ± 0.05	0.99	11.7 ± 0.7

Table 4.5: Summary of the electroanalytical performance of $ZnEu_2O_4$, $CuEu_2O_4$, and $CoEu_2O_4$ modified electrodes. Reported values include the slope of the calibration curve, the relative sensitivity, the coefficient of determination (R^2), and the limit of detection (LOD).

4.2.4 Ifosfamide Detection with CYP3A4

Following the same protocol described in the previous paragraph for cyclophosphamide detection with CYP2B6, dual electrodes modified with europium oxides and CYP3A4 were used for the electrochemical detection of ifosfamide. Both cyclic voltammetry (CV) and differential pulse voltammetry (DPV) showed enzymatic peaks around –400 mV, confirming the activity of the cytochrome P450 isoform CYP3A4. Also in this configuration, DPV provided a more sensitive response compared to CV.

As described previously, the calibration curves for all three materials, obtained after baseline subtraction, were calculated and are displayed together in Figure 4.11. For each material, three calibrations were carried out using three separate electrodes, and the curves shown represent the average responses along with their standard deviations.

It is important to note that for the ${\rm CoEu_2O_4}$ material, the calibration curve was evaluated only up to 80 $\mu{\rm M}$ because the sensor saturated at higher concentrations, as observed in the cyclophosphamide detection.

Table 4.6 summarizes the sensitivity, coefficient of determination (R^2) , and limit of detection (LoD) values calculated for the different materials.

Material + CYP3A4	$\begin{array}{c} \textbf{Slope} \\ (\mu \textbf{A}/\mu \textbf{M}) \end{array}$	$egin{aligned} ext{Relative} \ ext{Sensitivity} \ ext{(nA/(μM·mm}^2$))} \end{aligned}$	R-Square (COD)	${f LOD\ Mean}\ (\mu{f M})$
${\rm ZnEu_2O_4}$	0.006 ± 0.0006	1.10 ± 0.10	0.96	22.9 ± 1.5
$CoEu_2O_4$	0.011 ± 0.001	2.07 ± 0.26	0.95	15.7 ± 1.8
$CuEu_2O_4$	0.009 ± 0.0003	1.66 ± 0.05	0.99	12.7 ± 1.7

Table 4.6: Summary of the electroanalytical performance of $ZnEu_2O_4$, $CuEu_2O_4$, and $CoEu_2O_4$ modified electrodes. Reported values include the slope of the calibration curve, the relative sensitivity, the coefficient of determination (R^2), and the limit of detection (LOD).

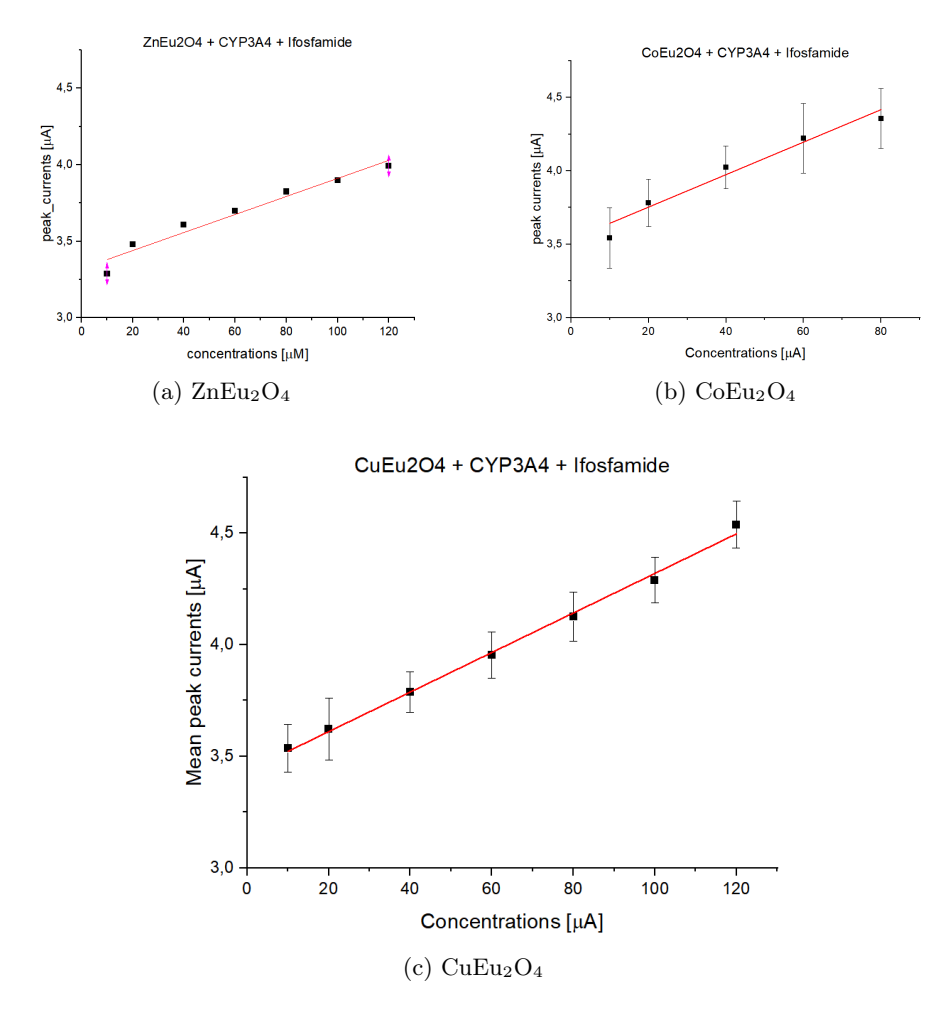
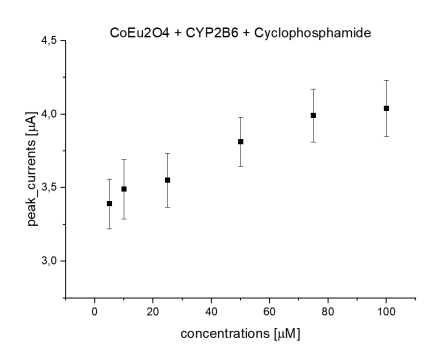


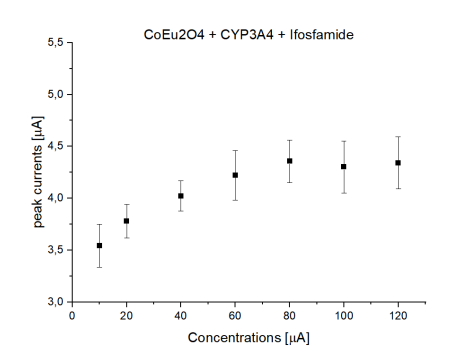
Figure 4.11: Calibration curves for the three europium spinel oxide materials: (a) $\rm ZnEu_2O_4$, (b) $\rm CoEu_2O_4$, and (c) $\rm CuEu_2O_4$ with CYP3A4 for ifosfamide detection.

4.2.5 Comparison of Spinel Europium Oxides

Among the three europium-based spinel oxides tested, $CoEu_2O_4$ demonstrated the highest sensitivity for both ifosfamide detection with CYP3A4 and cyclophosphamide detection with CYP2B6 however it saturated at high concentrations. The relative sensitivity values were $2.07 \pm 0.26~nA/\mu M/mm^2$ for ifosfamide and $2.10 \pm 0.23~nA/\mu M/mm^2$ for cyclophosphamide considering smaller measurement ranges respecting the pharmacological range chosen during the study .This is evident from Figures 4.12a and 4.12b showing peak currents versus concentrations. The corresponding limits of detection (LOD) were $15.7 \pm 1.8~\mu M$ for ifosfamide and $17.5 \pm 1.5~\mu M$ for cyclophosphamide, indicating good sensitivity but slightly higher signal variability compared to other materials.

 ${\bf CuEu_2O_4}$, while showing slightly lower sensitivity $(1.66\pm0.05~n{\rm A}/\mu{\rm M}/{\rm mm^2}]$ for ifosfamide and $1.37\pm0.05~n{\rm A}/\mu{\rm M}/{\rm mm^2}]$ for cyclophosphamide), exhibited the lowest LOD values $(12.7\pm1.7~\mu{\rm M})$ and $11.7\pm0.7~\mu{\rm M}$, respectively) and the highest linearity (${\bf R^2=0.996}$), suggesting more precise measurements at low analyte concentrations. ${\bf ZnEu_2O_4}$ presented the lowest sensitivity and highest LODs for both analytes, indicating it is the least efficient material among those tested.





(a) $CoEu_2O_4 + CYP2B6$ in cyclophosphamide (5–100 μ M).

(b) $CoEu_2O_4 + CYP3A4$ in ifosfamide (10–120 μ M).

Figure 4.12: Peak current vs. concentration for $CoEu_2O_4$ modified electrodes with the corresponding cytochrome P450 enzymes. (a) Cyclophosphamide with CYP2B6, (b) Ifosfamide with CYP3A4.

A summury of europium based spinel oxides is presented in 4.7. Since it is important that the sensor operates effectively within the pharmacological concentration range of the drugs to provide reliable measurements in clinical settings and taking into account all parameters summarized in Table 4.5 and 4.6. $CuEu_2O_4$ was selected for further testing and validation in human serum.

Material	Key characteristics
CoEu ₂ O ₄	Shows the highest sensitivity (2.07–2.10 nA/ μ M/mm²), but in a limited range.
CuEu ₂ O ₄	Exhibits the lowest LODs (11.7–12.7 μ M) and the highest linearity (R ² = 0.99). Sensitivity is slightly lower than CoEu ₂ O ₄ but stable and precise
ZnEu ₂ O ₄	Displays the lowest sensitivity (0.94–1.10 nA/ μ M/mm ²) and the highest LODs (\sim 23 μ M), with lower linearity

Table 4.7: Qualitative comparative summary of europium-based spinel oxides with CYP3A4 (ifosfamide) and CYP2B6 (cyclophosphamide).

4.3 Validation in Human Serum

Tests were conducted in human serum to evaluate the sensor performance in a complex biological matrix, better representing physiological conditions. The tests in serum were performed with ${\rm CuEu_2O_4}$ material, which was identified as the best based on previous evaluations. The electrodes tested were dual sensor electrodes, one bare working electrode and one modified with the material, both functionalized with enzymes. Two sets of three electrodes were used: one set with the enzyme CYP2B6 for cyclophosphamide detection, and another set with the enzyme CYP3A4 for ifosfamide detection.

The concentration ranges of the solutions used in serum were the same as those used in PBS, as shown in Table 4.8.

Drug	Concentration Range (µM)
Cyclophosphamide	0 (SERUM only), 5, 10, 25, 50, 75, 100
Ifosfamide	0 (SERUM only), 10, 20, 40, 60, 80, 100, 120

Table 4.8: Concentration ranges of cyclophosphamide and ifosfamide solutions tested in human serum.

In serum, only differential pulse voltammetry (DPV) was applied where a peak due to the CYP450 enzyme appears clearly at around 400 mV and increases with higher drug concentrations. Detectable peaks emerge starting at 25 μ M for cyclophosphamide and 40 μ M for ifosfamide.

Calibration curves were constructed following the some steps in the previous section , for both drugs and are presented e in Figure 4.13. It is evident that the standard deviations (std) are larger in the serum matrix, which is probably due to residual interference and variability introduced by the serum even after dilution.

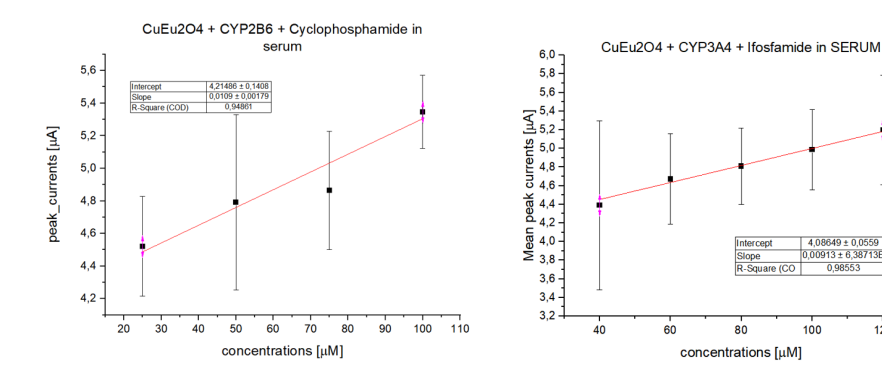


Figure 4.13: Calibration curves for cyclophosphamide (left) and ifosfamide (right) obtained from DPV measurements in human serum, showing linear response in the tested concentration ranges.

Electrode	Sensitivity $(nA/\mu M/mm^2)$	\mathbf{R}^2
$\overline{\mathrm{CoEu_2O_4} + \mathrm{CYP2B6} + \mathrm{CP}}$	2.04 ± 0.34	0.95
$CoEu_2O_4 + CYP3A4 + IFO$	1.71 ± 0.34	0.99

Table 4.9: Sensitivity and determination coefficients of DPV calibration curves for cyclophosphamide and ifosfamide in serum are shown in the table. The measurements were performed using three CuEu2O4 electrodes functionalized with CYP2B6 for cyclophosphamide detection and CYP3A4 for ifosfamide detection.

Conclusions and Future Perspectives

This thesis focused on the development of dual electrochemical biosensors based on europium spinel oxide nanoparticles doped with copper, cobalt, and zinc for the detection of important anticancer drugs, cyclophosphamide and ifosfamide. The study showed that these nanomaterials, synthesized via an autocombustion method, have structural and electrochemical properties that can be exploited in biosensor design. Detailed characterization using FESEM, XRD, and Raman spectroscopy confirmed the successful formation of uniform, crystalline spinel nanoparticles with defined morphology and chemical composition.

The electrochemical characterization revealed that the nanoparticles modified the electron transfer processes at the electrode interface. Using cyclic voltammetry at different scan rates, Laviron's model and the Randles-Sevčík equation allowed the determination of electron transfer coefficients and diffusion constants with enhanced values compared to unmodified electrodes. Electrochemical impedance spectroscopy further supported these findings by showing reduced charge transfer resistance on nanoparticle modified surfaces, confirming improved electron transfer kinetics.

Two types of sensors were developed by depositing these nanomaterials on commercial dual screen-printed carbon electrodes: sensors with only the metal oxides, and biosensors combining nanomaterials with the selective enzymes CYP2B6 and CYP3A4, which catalyze the metabolism of cyclophosphamide and ifosfamide, respectively. The results demonstrated that only the enzyme-functionalized sensors provided significant and reproducible responses toward the target prodrugs in phosphate-buffered saline. This highlights the crucial role of enzymatic activity in the detection mechanism.

Among the different doped europium oxides studied, CuEu₂O₄ showed the optimal performance, with good sensitivity, linear detection range, and stability in both buffer and human serum samples. The quantified sensitivities were $1.37\pm0.05\,\mathrm{nA/\mu M\cdot mm^2}$ for cyclophosphamide and $1.66\pm0.05\,\mathrm{nA/\mu M\cdot mm^2}$ for ifosfamide detection, which are promising for practical applications. Although cobalt europium oxide modified electrode exhibited higher sensitivity their sensor response saturated before reaching the chosen therapeutic concentration range of the drugs, limiting their practical utility.

In the future, research should focus on making the sensors more stable and selective when used with complex biological samples, by reducing interference from other substances in serum. It would be useful to detect more types of drugs and their metabolites by adding different enzymes or nanomaterials. Also, creating small, portable devices for easy and fast measurement of drug levels could help with personalized treatment. Moreover, since therapeutic treatments typically consist of drug combinations rather than single compounds, it is important for future sensors to be capable of simultaneously detecting multiple drugs. This capability would provide a more comprehensive and realistic monitoring of patient medication, improving the effectiveness of personalized therapies. Improving how enzymes are attached to the sensor surface and how the nanomaterials spread could make the sensors more reliable and last longer. Using better data analysis methods might help get clearer results from complex samples. Finally, testing the sensors for long term use and in real clinical conditions is important before they can be used outside the laboratory. In summary, this thesis demonstrates that europium spinel oxide nanoparticles, especially CuEu₂O₄, combined with specific metabolic enzymes form effective dual electrochemical biosensors for anticancer drug detection. Future developments aimed at personalized medicine and point of care diagnostics, contributing to safer and more effective chemotherapy treatments.

Bibliography

- [1] Jaya Baranwal et al. "Electrochemical sensors and their applications: A review". In: *Chemosensors* (2022).
- [2] Nelson R. Stradiotto, Hideko Yamanaka, and Maria Valnice B. Zanoni. "Electrochemical sensors: A powerful tool in analytical chemistry". In: *Brazilian Chemical Society* (2003).
- [3] Kevin Beaver, Ashwini Dantanarayana, and Shelley D. Minteer. "Materials approaches for improving electrochemical sensor performance". In: *The Journal of Physical Chemistry B* (2021).
- [4] Sandro Carrara. Bio/CMOS interfaces and co-design. Springer Nature, 2023.
- [5] Zahra Taleat, Alireza Khoshroo, and Mohammad Mazloum-Ardakani. "Screen printed electrodes for biosensing: A review (2008–2013)". In: Microchimica Acta (2014).
- [6] Dorothee Grieshaber et al. "Electrochemical biosensors—sensor principles and architectures". In: Sensors (2008).
- [7] Celine I. L. Justino, Teresa A. Rocha-Santos, and Armando C. Duarte. "Review of analytical figures of merit of sensors and biosensors in clinical applications". In: *TrAC Trends in Analytical Chemistry* (2010).
- [8] Jae Hyun Kim et al. "Technological advances in electrochemical biosensors for the detection of disease biomarkers". In: *Biomedical Engineering Letters* (2021).
- [9] George S. Wilson and Raeann Gifford. "Biosensors for real-time in vivo measurements". In: *Biosensors and Bioelectronics* (2005).
- [10] Bansi D. Malhotra et al. "Recent trends in biosensors". In: Current Applied Physics (2005).
- [11] V. V. Shumyantseva et al. "From electrochemistry to enzyme kinetics of cytochrome P450". In: *Biosensors and Bioelectronics* (2018).
- [12] Zahra Taleat, Alireza Khoshroo, and Mohammad Mazloum-Ardakani. "Screen printed electrodes for biosensing: A review (2008–2013)". In: Microchimica Acta (2014).

- [13] O. Dominguez Renedo, M. A. Alonso-Lomillo, and M. J. Arcos Martinez. "Recent developments in the field of screen-printed electrodes and their related applications". In: *Talanta* (2007).
- [14] Varnakavi Naresh and Nohyun Lee. "A review on biosensors and recent development of nanostructured materials-enabled biosensors". In: Sensors (2021).
- [15] I. G. Denisov et al. "Structure and chemistry of cytochrome P450". In: Chemical Reviews (2005).
- [16] C. Baj-Rossi, G. De Micheli, and S. Carrara. "P450-based nano-bio-sensors for personalized medicine". In: *Nanobiosensors* (2011).
- [17] B. Issa et al. "Magnetic Nanoparticles: Surface Effects and Properties Related to Biomedicine Applications". In: *International Journal of Molecular Sciences* (2013).
- [18] Kebede K. Kefeni, Titus A. M. Msagati, and Bhekie B. Mamba. "Ferrite nanoparticles: synthesis, characterisation and applications in electronic device". In: *Materials Science and Engineering B* (2017).
- [19] Josué Gonçalves et al. "Sensing performances of spinel ferrites MFe2O4 (M= Mg, Ni, Co, Mn, Cu and Zn) based electrochemical sensors: A review". In: Analytica Chimica Acta (2022).
- [20] D. Hernández-Ramírez et al. "Review—Trends on the Development of Non Enzymatic Electrochemical Sensors Modified with Metal-Oxide Nanostructures for the Quantification of Uric Acid". In: Journal of The Electrochemical Society (2021).
- [21] Thomas Girardet et al. "Spinel Magnetic Iron Oxide Nanoparticles: Properties, Synthesis and Washing Methods". In: *Applied Sciences* (2022).
- [22] Christoph Wenisch et al. "Europium(III)-Doped MgAl2O4 Spinel Nanophosphor Prepared by CO2 Laser Co-Vaporization". In: *Journal of the American Ceramic Society* (2016).
- [23] E. Dabbish et al. "Insights on cyclophosphamide metabolism and anticancer mechanism of action: A computational study". In: *Journal of Computational Chemistry* (2024).
- [24] F. Juma, H. Rogers, and J. Trounce. "Pharmacokinetics of cyclophosphamide and alkylating activity in man after intravenous and oral administration". In: *British Journal of Clinical Pharmacology* (1979).
- [25] E. Dabbish et al. "Insights on cyclophosphamide metabolism and anticancer mechanism of action: A computational study". In: Journal of Computational Chemistry (2024).
- [26] C. Baj-Rossi, G. De Micheli, and S. Carrara. "Electrochemical detection of anti-breast-cancer agents in human serum by cytochrome P450-coated carbon nanotubes". In: Sensors (2012).

- [27] Z. Huang, P. Roy, and D. J. Waxman. "Role of human liver microsomal CYP3A4 and CYP2B6 in catalyzing N-dechloroethylation of cyclophosphamide and ifosfamide". In: *Biochemical Pharmacology* (2000).
- [28] D. Lowenberg et al. "PharmGKB summary: Ifosfamide pathways, pharmacokinetics and pharmacodynamics". In: *Pharmacogenetics and Genomics* (2014).
- [29] Noémie Elgrishi et al. "A practical beginner's guide to cyclic voltammetry". In: Journal of Chemical Education (2018).
- [30] Henry S. White, Allen J. Bard, and Larry R. Faulkner. *Electrochemical Methods: Fundamentals and Applications*. Wiley, 2001.
- [31] B. Jill Venton and Dana J. DiScenza. "Voltammetry". In: *Electrochemistry* for *Bioanalysis*. Elsevier, 2020.
- [32] James L. Melville and Richard G. Compton. "The Simulation of Differential Pulse Voltammetry". In: *Electroanalysis* (2001).
- [33] Metrohm Autolab. Teachware Metrohm Autolab B.V. 2020.
- [34] Laviron. "General expression of the linear potential sweep voltammogram in the case of diffusionless electrochemical systems". In: *Journal of Electro*analytical Chemistry (1979).
- [35] Mallikarjun Madagalam et al. "Bismuth-Nanocomposites Modified SPCEs for Non-Enzymatic Electrochemical Sensors". In: *IEEE Sensors Journal* (2021).
- [36] Gurvinder Singh Bumbral and Rakesh Mohan Sharma. "Raman spectroscopy: Basic principle, instrumentation and selected applications for the characterization of drugs of abuse". In: *Egyptian Journal of Forensic Sciences* (2016).
- [37] Anwar Ul-Hamid. A Beginners' Guide to Scanning Electron Microscopy. Springer Nature, 2018.
- [38] T.-L. Chen et al. "Nonlinear pharmacokinetics of cyclophosphamide and 4-hydroxycyclophosphamide/aldophosphamide in patients with metastatic breast cancer receiving high-dose chemotherapy". In: *Drug Metabolism and Disposition* (1997).
- [39] J. Singer et al. "The pharmacokinetics and metabolism of ifosfamide during bolus and infusional administration: a randomized cross-over study". In: *British Journal of Cancer* (1998).
- [40] S. Mitchell et al. "Statistical overview of standard (IUPAC and ACS) and new procedures for determining the limits of detection and quantification". In: Pure and Applied Chemistry (1997).
- [41] P. Yamchumporn et al. "Study Ratio Between the CuO and Eu2O3 Concentrations on Electrical Resistivity, Seebeck Coefficient and Power Factor of CuEu2O4". In: *Integrated Ferroelectrics* (2021).

- [42] Irshad K. A. et al. "X-ray diffraction and Raman studies on Ho:Eu2O3". In: *Journal of Molecular Structure* (2019).
- [43] Vladimir Sepelák et al. "Mechanically Induced Reactivity of ZnFe2O4". In: (2015).
- [44] A. Jagannatha Reddy et al. "Combustion synthesis, characterization and Raman studies of ZnO nanopowders". In: (2012).
- [45] Samaila Bawa Waje et al. "X-ray diffraction studies on crystallite size evolution of CoFe2O4 nanoparticles prepared using mechanical alloying and sintering". In: (2016).
- [46] Moumita Ghosh, E. V. Sampathkumaran, and C. N. R. Rao. "Synthesis and Magnetic Properties of CoO Nanoparticles". In: (2005).
- [47] Raghvendra Singh Yadav et al. "Cation migration-induced crystal phase transformation in copper ferrite nanoparticles and their magnetic property". In: Journal of Superconductivity and Novel Magnetism (2016).
- [48] H. Hagemann et al. "Raman spectra of single crystal CuO". In: *Solid State Communications* (1990).
- [49] Raghvendra Singh Yadav et al. "Impact of grain size and structural changes on magnetic, dielectric, electrical, impedance and modulus spectroscopic characteristics of CoFe2O4 nanoparticles synthesized by honey mediated sol-gel combustion method". In: Advances in Natural Sciences: Nanoscience and Nanotechnology (2017).
- [50] Mallikarjun Madagalam et al. "Unraveling the Effect of the Chemical and Structural Composition of Zn x Ni1-x Fe2O4 on the Electron Transfer at the Electrochemical Interface". In: Small Structures (2023).

Acknowledgments

I would like to thank Professors Sandro Carrara and Alberto Tagliaferro for giving me the chance to work at the EPFL laboratories in Neuchâtel and at the Carbon Group at Politecnico di Torino.

I would like to thank Mattia Bartoli for his help and advice during my thesis project, as well as the BCI Lab for welcoming me and making my time there enjoyable. I want to thank Francesca Rodino for her constant support and for always being a kind and supportive supervisor throughout my work in the lab. Finally, I want to thank my friends and family for their encouragement and support throughout my studies.